Publication Year	2018
Acceptance in OA	2021-01-12T08:15:25Z
Title	VIRAC: the VVV Infrared Astrometric Catalogue
Authors	Smith, L. C., Lucas, P. W., Kurtev, R., SMART, Richard Laurence, Minniti, D., Borissova, J., Jones, H. R. A., Zhang, Z. H., Marocco, F., Contreras Peña, C., Gromadzki, M., Kuhn, M. A., Drew, J. E., Pinfield, D. J., BEDIN, Luigi
Publisher's version (DOI)	10.1093/mnras/stx2789
Handle	http://hdl.handle.net/20.500.12386/29677
Journal	MONTHLY NOTICES OF THE ROYAL ASTRONOMICAL SOCIETY
Volume	474

Mon. Not. R. Astron. Soc. **000**, 000–000 (0000) Printed Tuesday 4th July, 2017 (MN LaTeX style file v2.2)

VIRAC: The VVV Infrared Astrometric Catalogue

L.C. Smith[1⋆], P.W. Lucas[1], R. Kurtev, R. Smart, D. Minniti, et al....
[1] *Centre for Astrophysics Research, Science and Technology Research Institute, University of Hertfordshire, Hatfield AL10 9AB, UK*

July, 2017

ABSTRACT
We present VIRAC version 1, a full astrometric catalogue of the VVV survey for 312,587,642 unique sources averaged across all overlapping pawprint and tile images. The catalogue includes 119 million high quality proper motion measurements with a median proper motion uncertainty of 0.67 mas yr^{-1} in the $11 < K_s < 14$ magnitude range. 47 million of these have sub-1 mas yr^{-1} statistical uncertainties. The catalogue also includes 6,935 sources with quality-controlled 5 σ parallaxes with a median uncertainty of 1.1 mas. The parallaxes show fairly good agreement with the TYCHO-Gaia Astrometric Solution (TGAS), though Lutz-Kelker bias is a significant issue for measurements at 5 to 10 σ. The SQL database housing the data is made available via the web. We give example applications for studies of Galactic structure, nearby objects (low mass stars and brown dwarfs, subdwarfs, white dwarfs), Galactic clusters and kinematic distance measurements of YSOs. These include discovery of LTT 7251b, an L7 benchmark companion to a G dwarf with over 20 published elemental abundances and discovery of a bright L sub-dwarf, 2MASS 1256-6202, with extremely blue colours. Finally, we demonstrate why this catalogue remains useful in the era of GAIA. Future versions will be based on profile fitting photometry, use the GAIA absolute reference frame and incorporate the longer time baseline of the VVV extended survey (VVVX).

Key words:

1 INTRODUCTION

In recent years the astronomical community has undertaken several large projects that aim to measure the structure and dynamics of the Milky Way, e.g. the GAIA astrometric mission (Gaia Collaboration et al. 2016), the optical spectographs 4MOST (de Jong et al. 2016) and WEAVE (Dalton et al. 2016) and the infrared spectrographs APOGEE I-II (Majewski et al. 2015; Majewski, APOGEE Team & APOGEE-2 Team 2016) and MOONS (Cirasuolo et al. 2014). The VISTA Variables in the Via Lactea (VVV) survey (Minniti et al. 2010) complements this effort by providing time series K_s photometry of a 560 deg^2 region of the Galactic disc and bulge, much of which is hidden from the view of optical projects. Although originally planned to measure 3D Galactic structure using standard candles (RR Lyrae, red clump giants, Cepheids) it has become apparent that VISTA has excellent astrometric properties that enable proper motion measurements across the Galaxy, either using VISTA alone (Libralato et al. 2015; Cioni et al. 2016), or in combination with other datasets (Cioni et al. 2014) such as the Two Micron All Sky Survey (2MASS, Skrutskie et al. 2006).

VVV data comprise typically between 50 and 80 epochs of K_s photometry over five years (2010 to 2015). In addition, VVV includes two epochs of Z, Y, J and H photometry taken at the beginning and end of the survey. Each epoch is subdivided into independent images that are treated separately in our astrometry.

In this paper we present version 1 (V1) of the VVV Infrared Astrometric Catalogue (VIRAC), based on the standard products provided by the v1.3 pipeline of the Cambridge Astronomical Survey Unit (CASU). This VIRAC V1 catalogue provides *relative* proper motions and parallaxes for all stars for which they could be measured in the individual pointings (pawprints) of VVV. The catalogue will be made available in the VISTA Science Archive (VSA, Cross et al. 2012, see www.roe.ac.uk/vsa) and in the ESO Archive.

Following the release of the GAIA 2nd Data Release, the VVV team also plans to provide VIRAC V2, a deeper catalogue based on profile fitting photometry of the VVV dataset that will provide astrometry on the GAIA absolute reference frame. We will also explore the possibility of further increasing the depth of VIRAC using a shift-and-stack algorithm, as has been done by the ALLWISE project (Kirkpatrick et al. 2014). The VVV project has been extended by a new survey, *VVVX*, that continues to survey the original VVV area approximately 9 times up to 2020, while extend-

---

⋆ L.C.SMITH@herts.ac.uk

© 0000 RAS

ing the area to cover an additional 1100 deg^2 of the Galactic disc and bulge at 25-40 epochs. We plan to incorporate VVVX data into future astrometric products.

Here we describe our proper motion and parallax methodology and present initial results. These include nearby high proper motion stars and brown dwarfs and a simple illustration of how VIRAC can be used at large distances across the Milky Way. Our results include a complete catalogue of visually confirmed sources with proper motion, $\mu > 200$ mas/yr, complementing the VVV high proper motion catalogue recently published by Kurtev et al. (2017) for relatively bright stars with magnitudes $K_s < 13.5$.

In section 2 we describe the dataset and data selection. Section 3 details the source matching and the proper motion and parallax calculations. In Section 4 we describe our quality checks and quality flags for the proper motion catalogue, using internal self-consistency, visual inspection and comparison to both Tycho-GAIA Astrometric Solution (TGAS, Michalik, Lindegren & Hobbs 2015) and the results of Kurtev et al. (2017). This section also describes our table of visually confirmed high proper motion stars (the table itself can be found in the appendices) and new proper motion companions to TGAS stars. In Section 5 we describe the parallax catalogue and parallax quality checks using TGAS. In section 6 we describe discoveries of note from the parallax dataset and high proper motion sources. In Section 7 we demonstrate measurement of the Galactic rotation curve by averaging results for numerous stars and we mention additional uses for VIRAC in future.

2 DATA DESCRIPTION AND SELECTION

The VISTA Infrared Camera (VIRCAM) is the current largest near-infrared imager in astronomical use, consisting of sixteen 2048×2048 pixel mercury cadmium telluride arrays. The VISTA/VIRCAM combination gives a total viewing area of 0.6 deg^2 for each pointing or "pawprint" of the telescope. Detectors are placed in a 4×4 grid with spacing of 0.9 detector widths in the y direction and 0.425 detector widths in the x direction. The conventional tiling pattern used in VVV consists of six separate pawprints (three positions in x, two in y) that produce a filled "tile" covering $\sim$1.4×1.1°, with most positions observed twice due to the substantial overlap in the x direction. However, the six pawprints must be treated separately for precise astrometric work. VISTA and VIRCAM are described in great detail by Sutherland et al. (2015). Pipeline data reduction, catalogue generation and calibration of the photometry and astrometry are provided by the Cambridge Astronomical Survey Unit (CASU), see Lewis, Irwin & Bunclark (2010) and http://casu.ast.cam.ac.uk/surveys-projects/vista/technical. The VSA provides further processing (band-merging, production of light curves etc.) and curation of VVV data and makes it available to the community as an SQL database, providing an alternative to the ESO Archive.

The raw VVV FITS file catalogues were processed by a modified version of a fortran routine FITSIO_CAT_LIST (originally provided by CASU) ported to python. This modified version unpacks the binary tables for each extension in the FITS file and calculates calibrated magnitudes from the fluxes. It also flags and computes approximate magnitudes for saturated sources using a ring-shaped aperture, removes columns which are surplus to our requirements and outputs the resultant tables as a single extension FITS file.

The flux/magnitude aperture size we selected was aperMag2 (radius $= 1/\sqrt{2} \times 1''$). This relatively small aperture produces more reliable magnitudes in crowded fields (Lucas et al. 2008) than the more commonly used aperMag3, and aperMag2 benefits from more precise aperture corrections than aperMag1 (radius $= 1/2 \times 1''$).

For observation quality evaluation we stripped a subset of the header information from each catalogue, including airmass, seeing and the source counts for each chip. We compute the seeing for each pawprint as the median of the individual array seeing values multiplied by their plate scale (calculated from the astrometric fit coefficients of each array).

Coincident pawprints (pawprint sets) were identified by matching the telescope pointing coordinates of all pawprints using an internal sky match with a 20" matching radius with the TOPCAT software package (Taylor 2005). This yielded 2100 pawprint sets which corresponds to 6 pawprint sets for each of 346 VVV tiles and 12 pawprint sets for each of 2 VVV tiles (d015 and b390) for which the telescope pointing positions were > 1' from their usual positions at a number of epochs. These two tiles were subject to a change in pointing coordinates due to guiding problems caused by non-stellar profiles of guide stars used by the telescope guiding system. Because of this, observations before and after the change in pointing coordinates are treated separately by our astrometric pipeline, until the final stage of averaging over the independent astrometric solutions.

We rejected pawprints based on the following criteria:

- Deprecated (i.e. flagged as poor quality) by the quality control procedures used in the public data releases available at the VSA.
- Seeing $> 1.2''$.
- One or more of the 16 arrays contained fewer than 25% of the median source counts, computed for all spatially coincident arrays not already rejected.
- The median r.m.s. astrometric residual of reference stars used in the CASU pipeline global astrometric solution (FITS keyword: STDCRMS) across all arrays is greater than $0.2''$.
- The median average stellar ellipticity (FITS keyword: ELLIPTIC) across all arrays is greater than 0.2.

3 ASTROMETRIC METHOD

3.1 Source Matching

Many factors need to be considered when devising a suitable matching strategy across the many epochs of data for each pawprint set. With many epochs we are not limited by the quality of the worst epoch but we need to consider that not all sources will be detected at every epoch.

We settled on a strategy of identifying groups of epochs separated from other groups by at least 90 days, then identifying a primary epoch in each group (which we designate the P2 epoch). Most often the separations between groups correspond to the separations between observing seasons.

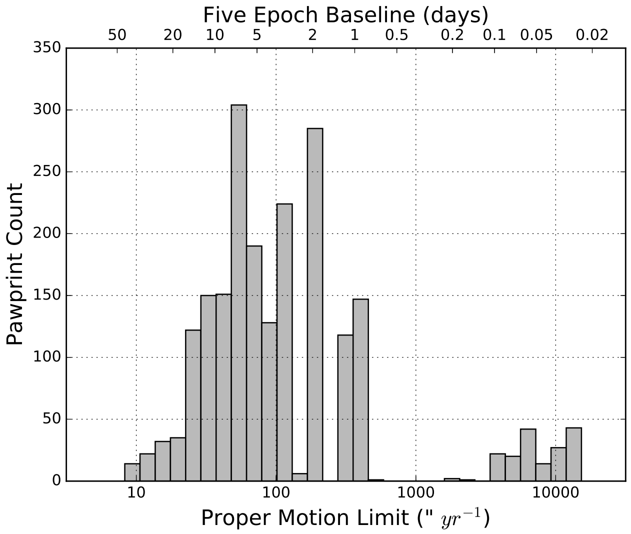

Figure 1. A histogram of the number of pawprints versus their maximum proper motion detection limit. The maximum proper motion detection limit comes from our $1''$matching radius and our requirement that a source be detected in one P2 epoch and at least four other epochs. The equivalent epoch baseline in days is shown on the upper x axis.

The P2 epoch in each group is the observation with the best seeing that also has higher than median source counts for observations in the group. The remaining epochs we refer to as secondary epochs. The P2 epochs from consecutive groups are then matched with a $1''$ OR match using the STILTS software package[1] (Taylor 2006). The secondary epochs are matched to the closest chronological P2 epoch with a $1''$match in STILTS such that all P2 epoch catalogue rows are returned matched to the closest secondary epoch row. Each secondary epoch row is matched only once and unmatched P2 epoch rows are also retained.

The main strengths of this matching process are as follows. For a source to be retained through matching it need only be detected in one of the P2 epochs. Clearly, for a proper motion to be measured we must have a second detection but this may come from any other P2 or secondary epoch. This means the theoretical maximum proper motion detection limit is constrained by the $1''$ matching radius and the shortest epoch baseline between any P2 epoch and any other epoch. We later reject all sources detected in fewer than 5 epochs, so in reality, our maximum proper motion detection limit is constrained by the shortest epoch baseline between any P2 epoch and its fourth closest additional epoch. For 99.7% of pawprints this value is less than 36.5 days, which is equivalent to a maximum proper motion detection limit of $10''\ yr^{-1}$ or greater with our $1''$ matching radius (see Figure 1). This is sufficient to include any very nearby stars or brown dwarfs in the VVV area.

3.2 Coordinate Transformation

For each pawprint set we select the observation with the best seeing as the overall primary epoch (which we designate the P1 epoch), to which we fit the remaining epochs. We select an initial pool of astrometric reference sources which meet the following criteria in the P1 epoch:

- $12.5 < Ks < 16.0$
- classified as stellar
- $\sigma_{Ks} < 0.15$ mag
- ellipticity less than 0.3
- Location > 6 pixels from the edge of the array in both the x and y dimensions

We split each array into a 5×5 grid of sub-arrays (25 sub-arrays per array, 400 per pawprint) and perform the coordinate fitting and transformation on this smaller scale. This helps to take account of smaller scale non-uniformity in the focal plane (see e.g. Libralato et al. (2015)). The fit of the transformation also incorporates astrometric reference sources from a 20 pixel wide boundary outside the sub-array. This boundary helps by providing some additional reference sources in more sparse regions. While this is not necessary in the majority of the VVV, which has very high source densities, we prefer to treat the entire survey in a homogeneous manner. Additionally, the 20 pixel boundary reduces potential edge-effects, though these should be minimal with the straightforward linear fit we use.

Linear transformations of array coordinates (x,y) for all epochs are fit to their respective P1 epochs using the CURVE_FIT function from the *optimize* package of the *SciPy* library. We apply the transformation, reject reference sources with residuals greater than 3σ and repeat the fit until the reference source set does not change.

3.3 Proper Motion and Parallax Fitting

For a proper motion measurement, the array coordinates vs. time are fit using a robust least squares method also provided by the CURVE_FIT function from the *optimize* package of the *SciPy* library. For the robust aspect, we used the Trust Region Reflective algorithm with an *arctan* loss function and the default *f_scale* parameter. Testing of the different loss functions and *f_scale* parameters on various VVV tiles indicated that while there was little difference between them, the *arctan* loss function produced marginally lower statistical uncertainties while still producing consistent results between the overlapping areas of adjacent pawprint sets. Comparison with an unweighted least squares fit shows that this robust method usually delivers essentially the same result as the latter. The main effect is to improve results for sources having unusually large residuals to the fit. The fit on each axis produces a proper motion, uncertainty and the epoch 2012.0 position in the P1 array coordinate frame. We experimented with calculation of a χ^2_{red} goodness of fit statistic for every solution but we found that the positional uncertainties at each epoch were not sufficiently well defined to do this accurately, especially for bright stars.

We perform a zenith polynomial projection of these positions, proper motions and uncertainties in the P1 epoch array coordinate frame using the astrometric parameters con-

---

[1] We found that when performing an internal match of crowded UKIDSS or VISTA catalogues a $1''$ matching radius typically returned only self-matches whereas $> 1''$matching radii returned significant numbers of additional matches.

tained in the header of the original FITS file catalogue of the P1 epoch.

We fit parallaxes only for sources with proper motion greater than 20 mas yr^{-1} and detections at more than 10 epochs. We first perform the zenith polynomial projection of all positions and uncertainties as before and then fit their χ and η positions in the tangent plane to the parallax equations in the two dimensions using the same procedure and parameters as for the proper motion fits. This produces parallaxes, proper motions and epoch 2012.0 positions in both dimensions.

It's important to note that for the moment we have not corrected for the average motion of the astrometric reference sources used. All proper motions and parallaxes are therefore relative to the average motion of sources within a few arcminutes. Figure **??** shows that the difference in average motion of partially overlapping reference frames is essentially indistinguishable. Care must be taken however, if one wishes to use these data to e.g. investigate Galactic motion across larger scales (see Section 7). For practical purposes, the differences can be neglected on scales of approximately a VVV tile.

4 PROPER MOTION RESULTS

4.1 Self-Consistency

The VVV observation method enables a check for self-consistency between overlapping pawprint sets. Overlaps on the sky between pawprint sets are either between different arrays or different sections of the same array, in different parts of the focal plane. Since the volume of data is so great we select a sample of sources from tiles b216 (outer bulge), b332 (inner bulge, very high source density), d069 (inner disk, containing the Westerlund 1 compact young cluster) and d079 (outer disk) to test self-consistency. On these tiles we perform a $1''$ internal match on their 2012.0 positions to identify coincident detections of sources between multiple pawprint sets. We compare proper motions for sources with solutions in two pawprint sets and no proper motion error flags (see Section 4.2) and find that in each case the random errors in the proper motion measurements are described well by Gaussian distributions with the statistical uncertainties provided by CURVE_FIT.

4.2 Proper Motion Quality Flagging

Figure 2 shows the magnitude vs. proper motion uncertainty range for one pawprint set of VVV tile b216. Note the rapid increase in proper motion uncertainties at the bright and faint end, and the spread due to some sources in the middle with uncharacteristically large proper motion uncertainties for their magnitudes. For individual pawprint sets, we use a proper motion error flag, *epm flag*, that identifies these regions, in which reliability of proper motion measurements is generally low. This is most often a result of saturation of bright stars, low signal to noise ratio for faint stars, or most notably blending, as evidenced by relatively high ellipticity of sources in these regions (see Figure 3).

After averaging the multiple solutions for each source (see Section 4.3) the *epm flag* information is used to set a simple *reliable* flag (1 is reliable, 0 is not) to facilitate selection of the most reliable VIRAC proper motion measurements.

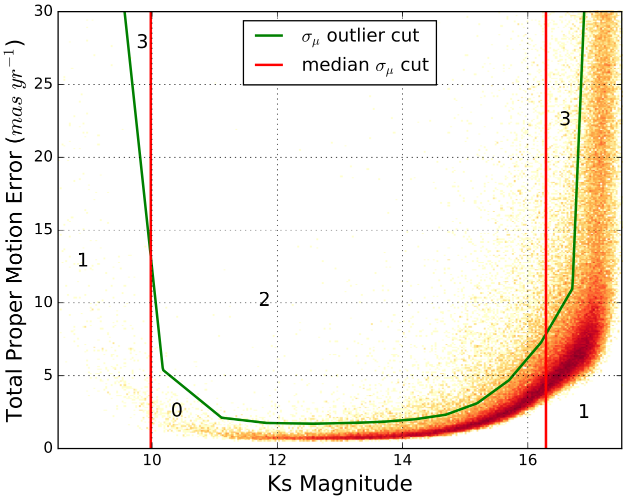

Figure 2. A log-scale 2d histogram showing proper motion uncertainty vs. magnitude for one pawprint set of tile b216 before averaging of measurements from overlapping pawprint sets. Note the rapid increase in proper motion measurement errors at the bright and faint limits, and the region of sources in the middle of the plot with unusually large proper motion uncertainties for their magnitude. The red lines show the magnitude range outside which we flag poorly measured sources (epm flag=1). The green line is the trace above which we flag sources as proper motion uncertainty outliers (epm flag=2). The numbers indicate the epm flag assigned to each region (the overlap of epm flag=2 and epm flag=1 gives epm flag=3).

To define *epm flag* for each pawprint set, we group sources by K_s magnitude in bins with 500 sources. Bins narrower than 0.5 mag are joined with neighbouring bins. We interpolate over the median proper motion uncertainties vs. median magnitudes for each group and identify the bright and faint limits outside which the median proper motion uncertainty exceeds 5 mas yr^{-1}. These represent the points at which the reliability of the results significantly decreases and such results are given *epm flag*=1. We also identify sources in each bin with proper motion uncertainties larger than the median proper motion uncertainty plus three times the spread, defined as the larger of 0.3 mas yr^{-1} and the median absolute deviation. Sources with proper motion uncertainty above this threshold, determined by interpolation of the thresholds across adjacent bins are given *epm flag*=2. The 0.3 mas floor is imposed in order to avoid flagging sources with errors that are no more than about double the typical error in the magnitude bin. In cases where both conditions are true we give sources *epm flag*=3. Figure 2 illustrates these selections made on one pawprint set of tile b216.

4.3 The Catalogue: Averaged Proper Motions

The tile and pawprint pattern of the survey is such that, with the exception of the very edges of the survey, all sources should be observed in at least two pawprint sets

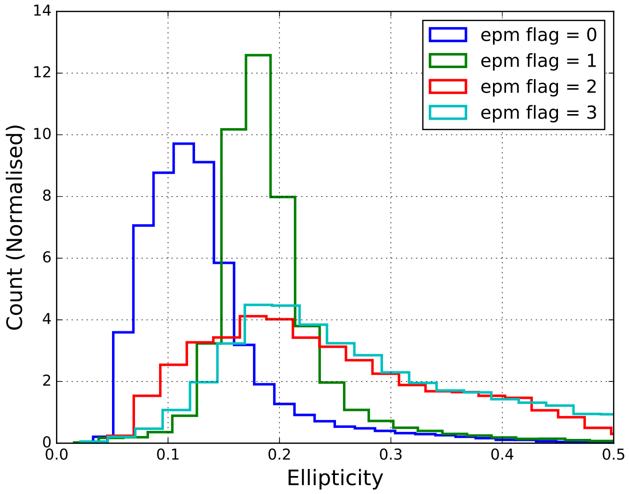

Figure 3. The ellipticity distributions of the separate resultant groups from the epm flagging routine of a single pawprint set of tile b216. Sources with an epm flag greater than 0 tend to have a higher ellipticity (suggestive of blending). Only sources with *epm flag* = 0 in all pawprints sets, and solutions in at least two pawprint sets, are given the *reliable* flag, see Section 4.3.

and therefore have a proper motion measurement in each. Additionally, due to the matching method we employ, some sources (e.g. faint, or very high proper motion stars) are not matched between consecutive P2 epochs and hence will also have a proper motion measured for multiple epoch groups within each pawprint set. To produce a catalogue of unique sources we identify groups of proper motion measurements by matching epoch 2012.0 positions to within $1''$, and average their proper motions using inverse variance weighting.

For each proper motion measurement, we report a K_s magnitude and uncertainty as the median and median absolute deviation (respectively) across all epochs that go into the proper motion measurement. For a source morphological classification we report the modal classification across those epochs. When we come to combine multiple measurements we give the inverse variance weighted average K_s magnitude and simply the number of proper motion measurements that have a modal stellar classification. The epm flags applied to each proper motion measurement are retained as counts, these are incorporated into a simple '*reliable*' flag. To be flagged as '*reliable*' a source must have a minimum of two proper motion measurements, all proper motion measurements must be from different pawprint sets, and there must be no error flags set for any proper motion measurement.

The combination of multiple proper motion measurements as above yielded 312,587,642 unique sources. Figure 4 shows the area covered and the source density and compares this to the Gaia DR1. Figure 5 shows proper motion uncertainty vs. magnitude distribution of the 119 million sources we consider to have the most reliable proper motions.

4.4 Comparison to a Reliable Proper Motion Sample

Kurtev et al. (2017) produced a visually confirmed sample of 3003 proper motion sources in the VVV area. For most sources they provide a 2MASS to VVV proper motion solution, covering a time baseline between 10 and 15 years. Their sample covers proper motions typically in the range 50–1000 mas yr^{-1}, and magnitudes from the brightest end of the VVV survey to $Ks \approx 13.5$. We removed η Sagittarii (source 2679) from the Kurtev et al. (2017) list as it is far too bright for any meaningful VVV detection (2MASS $K_s = -1.55$) and a further 151 sources for which proper motion was not given in their catalogue because their inclusion was based on previous proper motion measurements. Among the remaining sources we removed a further 4 duplicates: 1064/1065, 1134/1135, 1892/1893, 2394/2395. This left a total of 2847 sources which we should be able to recover in VIRAC. On crossmatching this list to our full results table (i.e. allowing sources not flagged as reliable) we recover all 2847 objects. Figure 6 shows the Kurtev et al. (2017) 2MASS-VVV total proper motion versus those of VIRAC for these objects.

We used this sample of 2847 bona fide high proper motion stars to evaluate our *epm flag* system, at least for the brighter end of our results. Figure 7 shows the breakdown of sources with any *epm flag* by magnitude. As one might expect, sources at the very brightest end of the survey have an *epm flag* indicating that their magnitude bin has median proper motion uncertainty greater than 5 mas yr^{-1} (*epm flag*=1) consistent with them saturating. The presence of many sources with an *epm flag*=2, meaning their proper motion uncertainties are significantly higher than normal for their magnitude is interesting. We visually inspected a sample of these sources ourselves and found that overwhelmingly the reason for their higher than normal proper motion uncertainties was blending with a background source. Another reason for *epm flag*=2 to be set for high proper motion sources is that many will have significant parallactic motion that would cause large scatter about a linear fit of position vs time (i.e. proper motion alone). This suggests that if one is looking for a *complete* selection of sources it is advisable to ignore our source reliability flag and include sources with *epm flag*=2.

4.5 Visually Confirmed High Proper Motion Stars

To assess the reliability of high proper motion source detections we selected sources with at least two proper motion measurements, proper motion, μ, measured with at least 5σ significance and $\mu > 200$ mas yr^{-1}. We rejected the very brightest and very faintest sources (sources with an *epm flag* = 1 or 3 in any proper motion measurement, see Section 4.2) but we retain sources with *epm flag* = 2 in one or more solutions (hence not flagged as *reliable*) so as to include sources that might otherwise be excluded due to parallactic motion or blending. This yielded 14,921 sources. Their proper motion uncertainty vs. magnitude distribution is shown in Figure 8 for the 6,796 with $\sigma_\mu < 30$ mas yr^{-1}. We visually inspected the 687 sources in this sample with $\sigma_\mu < 10$ mas yr^{-1}, of which 255 have *epm flag*=2 and would be expected to be less reliable. The 687 sources are identified in Figure 8 by pluses and crosses for those identified as genuine and false respectively.

All of the 432 "reliable" sources with *epm flag* = 0 were visually confirmed as genuine, save for one ambiguous case. This shows that this citerion is indeed useful for making

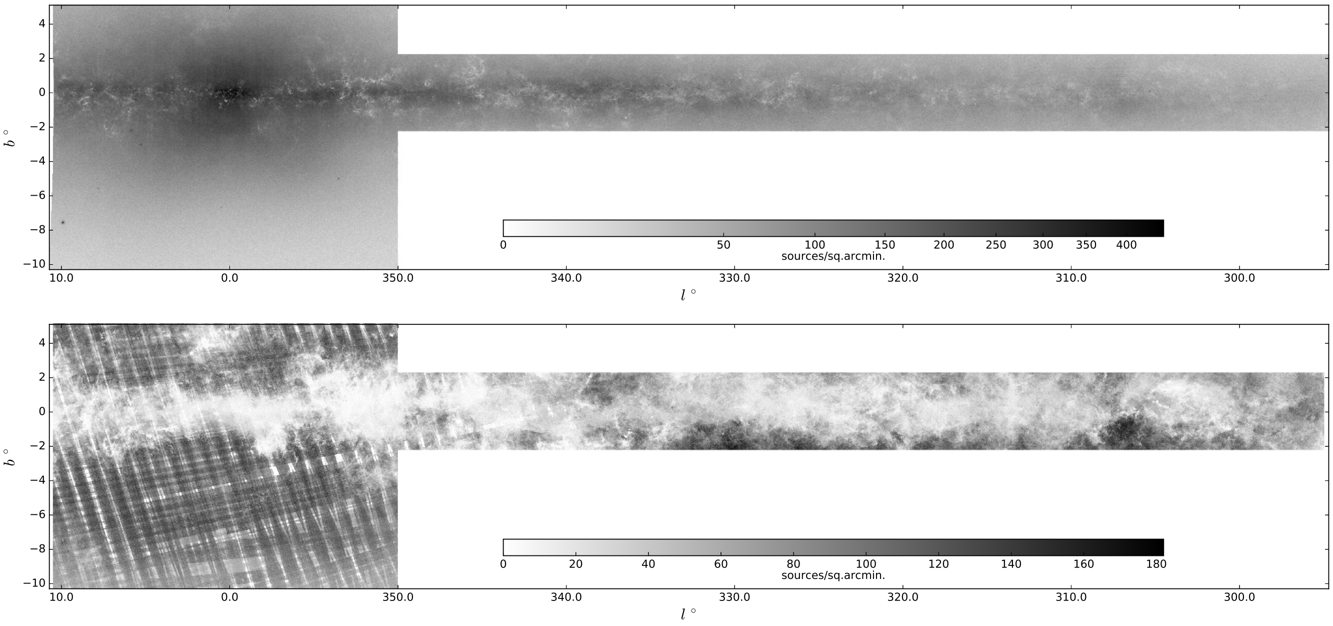

Figure 4. *upper:* Our VVV proper motion catalogue area coverage and $10 < Ks < 16$ source density. *lower:* The Gaia DR1 source density in the VVV survey area for comparison.

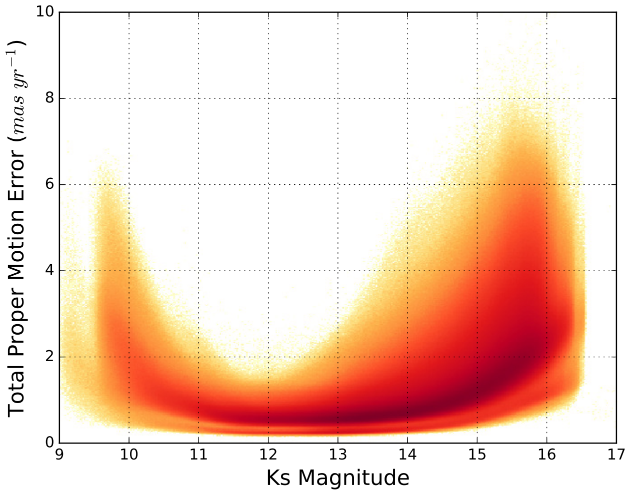

Figure 5. Density plot of Ks magnitude vs. uncertainty on the total proper motion of sources with detections in multiple pawprints and flagged as *reliable* (see Section 4.2). We consider this to be a reasonably reliable selection of proper motion measurements encompassing 119 million sources, 47 million of which have sub-1 mas yr^{-1} proper motion uncertainties. The track of sources visible underneath the main body is formed by 8 high cadence bulge tiles with several hundred epochs and very precise proper motions.

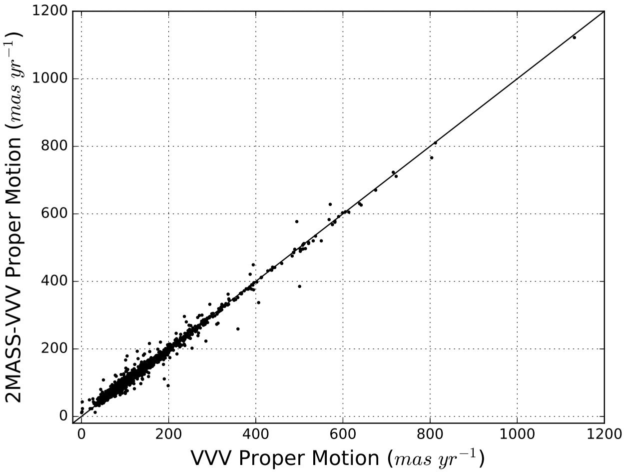

Figure 6. Our VVV total proper motions vs. the 2MASS + VVV total proper motions of Kurtev et al. (2017) for the 2847 sources recovered from their high proper motion catalogue of bright stars.

a reliable selection. The ambiguous source emerged from a blend with a background source over the 2010-2015 period: it appears to have a genuine motion but could perhaps be explained as a gradually brightening variable star.

Figure 8 shows that the catalogue contains a locus of candidate high proper motion sources at faint magnitudes with large proper motion errors and *epm flag*=2 in one or more solutions (due to the large proper motion uncertainties for their magnitude bin). Our visually inspected sample grazes the bottom of this distribution of sources: we found that all sources inspected which might reasonably be considered to be part of this group had false motions, predominantly due to mismatching caused by blending. Note that a gradual shift from predominantly genuine to predominantly false occurs at $\sigma_\mu \approx 5$ mas yr^{-1}, see the lower panel of Figure 9. The presence of genuine high proper motion sources with and without *epm flag*=2 in Figure 8 again highlights the need to ignore this particular flag if a complete selection is required.

All 555 visually confirmed high proper motion sources

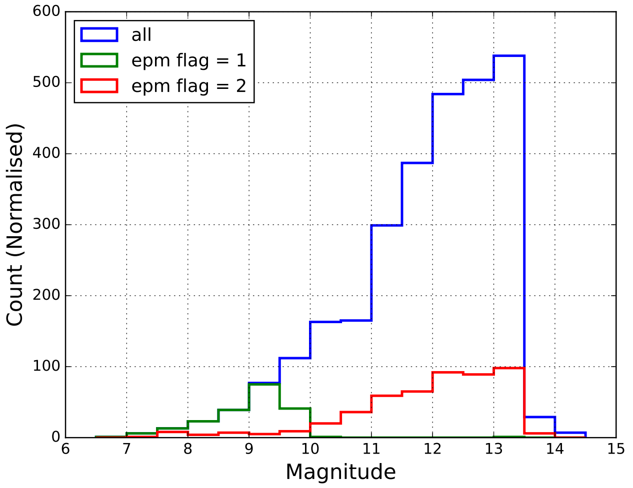

Figure 7. The breakdown of our epm flags by magnitude for known genuine high proper motion sources in common with the Kurtev et al. (2017) search. A source need only have an *epm flag* for a single proper motion measurement to be included in that histogram. Note that *epm flag*=3 indicates both *epm flags* 1 and 2 for a proper motion measurement so we have included such cases in both epm flag histograms. The blue histogram shows the breakdown of all 2847 sources by magnitude.

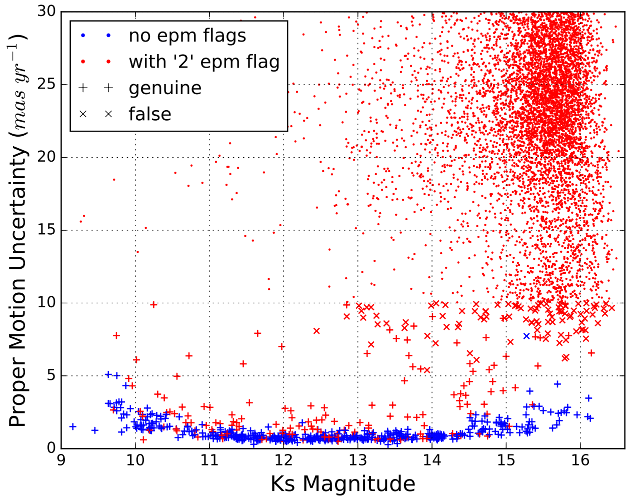

Figure 8. Proper motion error vs magnitude for the 6,796 sources with $\mu > 200$ mas yr^{-1} and $\sigma_\mu < 30$ mas yr^{-1}. Sources with $\sigma_\mu < 10$ mas yr^{-1} were visually inspected. Genuine high proper motion sources are identified by pluses, false high proper motion sources by crosses. Blue points are those flagged as 'reliable', red points allow *epm flag* = 2.

with $\mu > 200$ mas yr^{-1} and $\sigma_\mu < 5$ mas yr^{-1} are presented in Table A1.

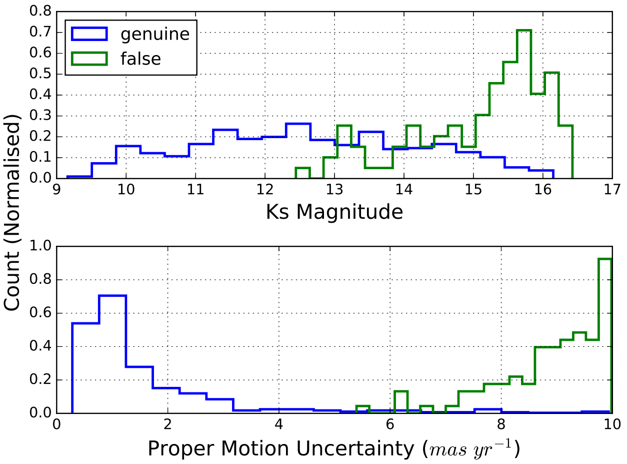

Figure 9. The Ks magnitude and proper motion uncertainty distributions of the sample of the 687 sources with $\mu > 200$ mas yr^{-1} and $\sigma_\mu < 10$ mas yr^{-1} that we visually inspected.

4.5.1 TGAS Common Proper Motion Companions

We undertook a search for common proper motion companions to TGAS proper motion sources. Since the probability of chance alignments of unrelated sources with similar motions falls as proper motion increases we select only TGAS sources with $\mu > 100$ mas yr^{-1}. We match this TGAS sample to a selection of our VIRAC sources with motions measured at $> 5\sigma$ significance, allowing *epm flag* = 0 or 2. We find 199 matches with separation less than $300''$ and proper motion consistent to within 50 mas yr^{-1} in both dimensions. To attempt to quantify the probability that each match is a chance alignment of unrelated objects we count TGAS sources in an annulus ($r_{in} = 5'$, $r_{out} = 120'$) around the VVV component of the match which have a proper motion agreement as good or better than that of the match. We then divide this count by the ratio of the area of the annulus and the area of a circle with radius equal to the original match separation to approximate the number of expected chance alignments within this radius. This method assumes that there will be no genuine companions outside $5'$. For the closest pair at d=36 pc, $5'$ is a projected separation of 10800 au; known systems with separations wider than this are rare. We reject any pairs with a number of expected chance alignments greater than 10^{-4}, and any whose projected separation at the distance of the TGAS source is greater than 10000 au.

This left 49 promising common proper motion companion candidates. We visually inspected the VVV component of each pair and found: 11 that are TGAS detections of the VVV source (these were all candidates with separation less than $1''$), 10 for which the VIRAC high proper motion is false (note that these were all cases with an *epm flag*=2 for one or more of their individual proper motion measurements), and 28 which have genuine high proper motion and are therefore bona-fide common proper motion companions. Table C1 lists these 28 bona-fide VVV common proper motion companions to TGAS sources.

A search of SIMBAD and the literature indicates that three of these systems are known: TYC 7365-318-1 AB was identified by Kurtev et al. (2017), and L 149-77 AB and L 200-41 AB were identified by Ivanov et al. (2013). Note that the BCircini system identified by Smith et al. (2015) does not appear in this list since BCircini does not appear in TGAS. The remaining 25 common proper motion pairs were previously unidentified. Of particular note are two of the systems: the CD-53 6250 AB system, a pre-main sequence K0IV primary star (Torres et al. 2006) and an X-ray detected secondary (we believe CD-53 6250 B is source 22 of Chen et al. 2008 table 1); and the LTT 7251 AB high contrast pair, a G8V primary with a low mass companion (see Section 6.1.2).

4.5.2 Very high proper motion candidates

In addition to the sample visually inspected in Section 4.5 we also searched for very high proper motion objects with still reasonable proper motion uncertainties, and for common proper motion companions to Proxima Centauri.

We identified four sources with $\mu > 1'' \; yr^{-1}$, σ_{mu} <30 mas yr^{-1} and a minimum of two proper motion solutions that each have *epm flag* = 0 or 2. Of these four sources, one was genuine. See Section 6.1.3 for details.

Our nearest stellar neighbour, high proper motion star and recently confirmed planet host (Anglada-Escudé et al. 2016) Proxima Centauri lies in the VVV survey footprint. We identified 163 sources that were within $128'$[2] of the van Leeuwen (2007) position of Proxima Centauri that also had a proper motion within $\pm\, 1'' \; yr^{-1}$ of the van Leeuwen (2007) proper motion for Proxima Centauri (-3775.75 ± 1.63 and 765.54 ± 2.01 in $\mu_{\alpha\cos\delta}$ and μ_δ respectively). This sample had no other selection criteria applied to it. We visually inspected the 163 sources but none had a genuine proper motion. This complements a recent dedicated VVV search for companions to this star by Beamin et al.(2017, submitted).

4.5.3 Reduced Proper Motion

In lieu of parallax measurements for all sources, and since proper motion scales as the inverse of the distance (with a few exceptions), we can use reduced proper motion to estimate luminosity of objects. Where H_{K_s} (reduced proper motion in the K_s band) is:

$$H_{K_s} = K_s + 5\log\mu + 5$$

Figure 10 shows the H_{K_s} vs. K_s for the 3200 visually confirmed VIRAC high proper motion sources and includes those VIRAC sources identified by Kurtev et al. (2017). We compare this to figure 5 of Kurtev et al. (2017) and note that we sample significantly fewer giant stars. This is likely due to Kurtev et al. (2017) including previously known proper motion sources, which include sources too bright to be measured by VIRAC.

5 PARALLAX RESULTS

5.1 Quality Control Cuts

Parallax uncertainty (averaged between pawprint sets) vs. Ks magnitude for sources with detections in two or more pawprint sets and parallax measured at greater than 5σ are shown in Figure 11 (upper panel). Note the swathe of negative parallaxes (in red on the plot) with large uncertainties and generally faint magnitudes. Since negative parallaxes are clearly not physical but due to random scatter in the measured parallax about true values typically near zero, we expect the roughly equal number of positive parallaxes in the same region of the plot to also be unreliable measurements. The dearth of negative parallaxes in the lower region of the plot indicates our locus of reliable measurements. We attempt to select only reliable parallax measurements as follows.

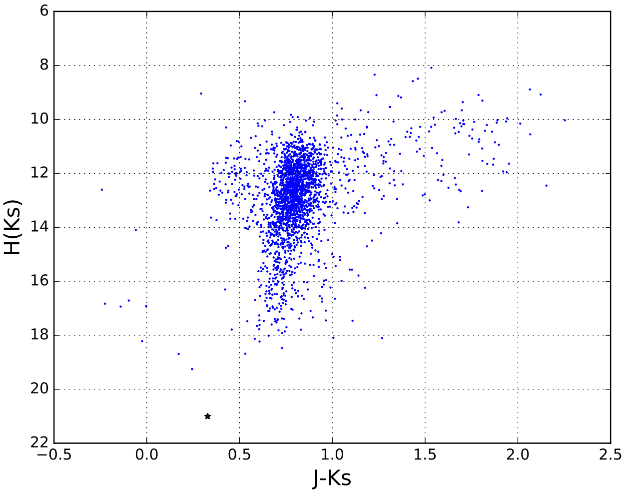

Figure 10. A reduced proper motion diagram of sources drawn from the 3200 visually confirmed high proper motion sources from VIRAC and Kurtev et al. (2017). We use our proper motion, median K_s magnitudes across all proper motion epochs and VVV DR4 tile catalogue J band photometry from the VSA. The 2263 sources in this plot comprise all those with $K_s < 20$,$J < 20$ and $K_s > 10$ (to minimise saturation effects), stellar J band morphological classification and 5σ proper motion. The high proper motion source 2MASS J12564352-6202041 is also shown (see Section 6.1.3.

Testing indicated the following requirements reduced the number of sources in the upper part of the plot significantly:

- $\geqslant 5\sigma$ inverse variance weighted average parallax.
- Parallax measurements from a minimum of pawprint sets.
- The two highest weighted measurements agree within 2σ and 10 mas, are positive, and each measured with at least 2σ significance.
- Mean ellipticity (across all epochs) is less than 0.2.

To this selection we apply a similar set of cuts to the epm flag = 0 selection above (see Section 4.2), albeit applied after the averaging of measurements from separate pawprints (including pawprints in adjacent tiles) and across the entire survey at once. Since the parallax dataset is smaller we reduce the width of the magnitude bins to 50 sources. Sources in a magnitude range where the median parallax uncertainty is greater than 5 mas, and those with parallax uncertainty greater than the median for their magnitude plus three times the spread (defined as the larger of either 0.3 mas or the median absolute deviation for their magnitude) are flagged as unreliable. The resultant selection of 6935 "reliable" parallax measurements are shown in Figures 11 (lower panel) and 12. The selection is shown in Table B1.

---

[2] Approximately 10,000 AU at the distance of Proxima Centauri

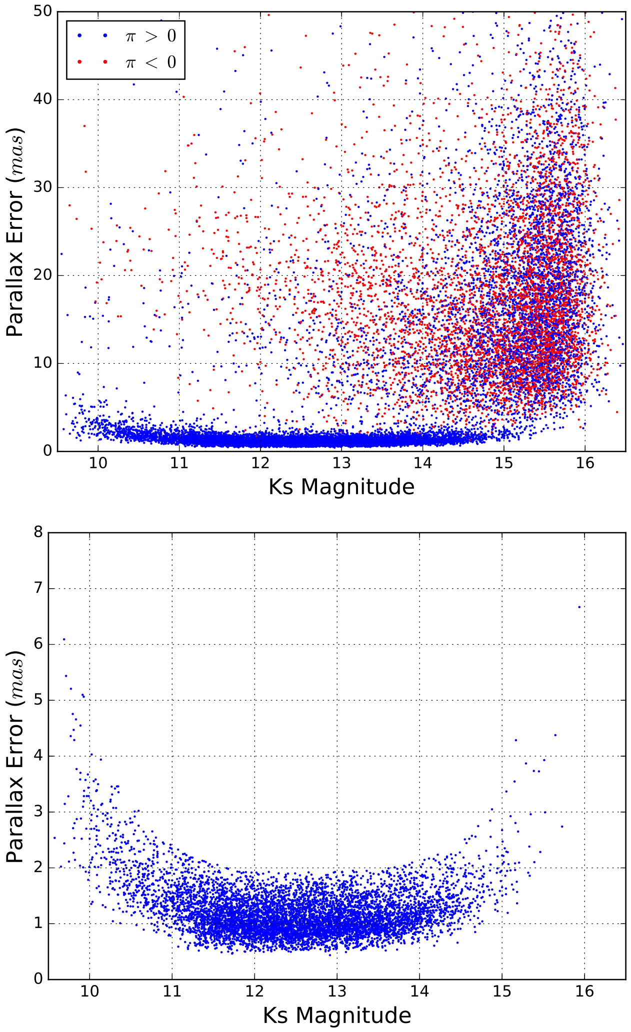

Figure 11. *upper*: Parallax uncertainty vs. Ks magnitude for sources with detections in two or more pawprints. Only sources with parallaxes measured at greater than 5σ significance are shown. Blue points are positive parallaxes, red points are negative parallaxes. Since negative parallaxes are not physical, caused by random scatter about true values near zero, we expect the roughly equal number of positive parallaxes in the same region of the plot to be unreliable also. The dearth of negative parallaxes in the lower region of the plot indicates our locus of reliable measurements. *lower*: Our subset of 6935 sources from the upper panel which we deem a reliable selection (see text for details) of parallax measurements.

5.2 Comparison to TGAS parallaxes

Sources common to TGAS and the VIRAC parallax selection are few. To increase the comparable sample we identify TGAS stars with fainter common proper motion companions in VVV and reason that these should have near identical parallaxes. To identify likely genuine companions we match the two catalogues with a $5'$ radius and proper motion agreement within 20 mas yr^{-1} in both $\alpha \cos\delta$ and δ. We quantify the probability that each match is a chance alignment of unrelated objects using a procedure identical to that described in Section 4.5.1. Note that this sample implicitly includes the few sources common to both catalogues.

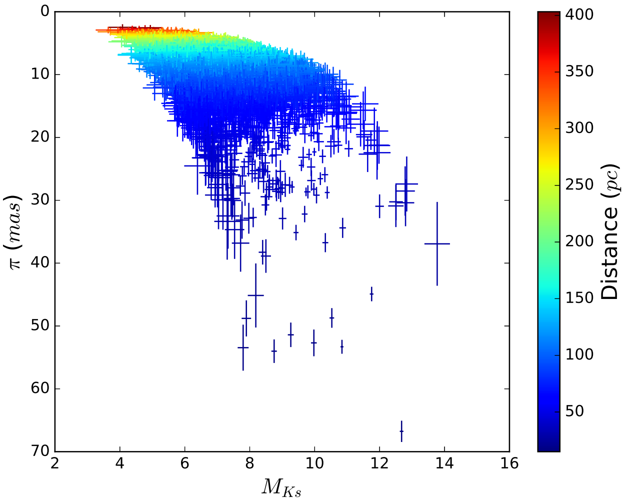

Figure 12. Absolute Ks magnitude vs. parallax for the 6935 5σ parallaxes.

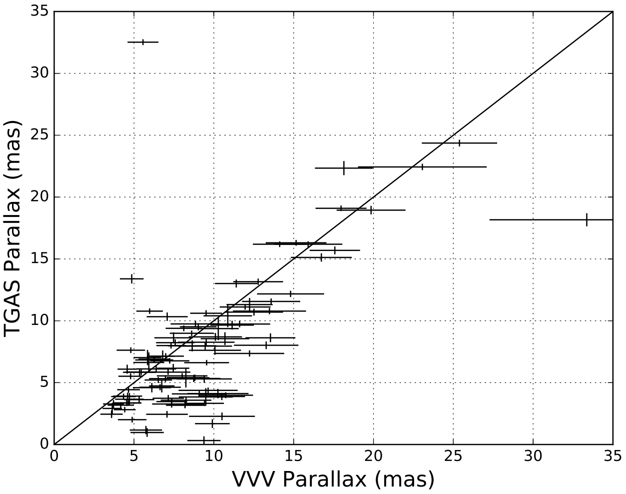

Figure 13. Comparison of VIRAC and TGAS parallax measurements for 102 common proper motion pairs identified by matching the two catalogues. The agreement is generally good. We attribute the group of sources with small TGAS parallaxes and larger VIRAC parallaxes to Lutz-Kelker bias in the VIRAC results, since the TGAS parallaxes are more precise. Lutz-Kelker bias is expected to be important in parallax surveys with significant uncertainties.

Figure 13 compares the TGAS parallaxes with those in the VIRAC for the 102 common proper motion matches with an expected incidence of chance alignment below 10^{-4}. The agreement is generally good. We attribute the increase in low parallax TGAS objects with higher VIRAC parallaxes to Lutz-Kelker bias (Lutz & Kelker 1973), since these are at the level of only just having 5σ parallax measurements in the VIRAC. (Lutz-Kelker bias is the scattering into a low precision parallax sample of more distant stars with parallax meaurements in the wings of the error distribution, owing to the very large number of stars in the large volume outside the typical distance limit of the survey.)

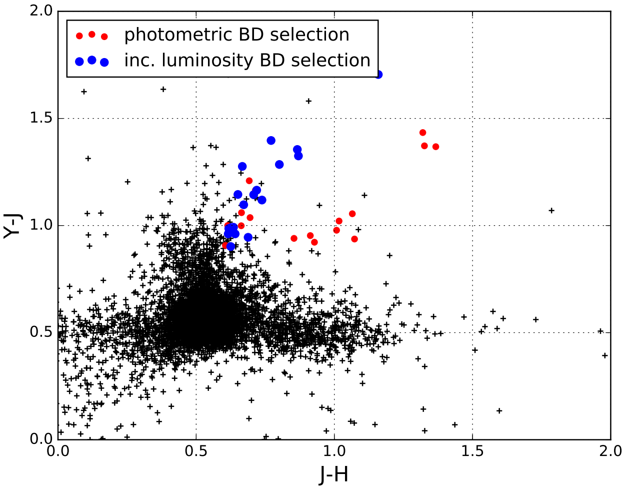

Figure 14. $J-Ks$ vs. $Y-J$ for the sources in the VIRAC parallax selection with YJHK detections. Highlighted are the 35 sources which meet our colour selection criteria for L0-T2 dwarfs (circles), those that also meet our luminosity selection criteria are highlighted in blue.

6 DISCOVERIES

6.1 L Dwarfs

One obvious use of the a near-infrared parallax catalogue is the identification of ultracool dwarfs. Even relatively luminous early L-type dwarfs are only visible out to distances of order 100 pc in wide field near-infrared surveys with modest integration times. For this reason, brown dwarfs detected in the VVV survey will often have a measurable parallax, as previously demonstrated by Beamín et al. (2013) and Smith et al. (2015).

We use a set of simple colour selections based on VVV photometry (which are all provided in VIRAC) and the extent of the M dwarf colours tabulated in Rojas-Ayala et al. (2014):

$Y-J>0.9$,
$J-H>0.6$,
$H-K>0.44$,

and require each of these to be met to be considered a candidate. Further, if a candidate is detected in the Z band we require $Z-J>1.3$ based on the brown dwarf selection of Lodieu et al. (2007). These colour selections correspond approximately to brown dwarfs in the subtype range L0-T2, and identify 35 candidate objects (see Figure 14). The addition of parallax information also allows us to discriminate based on intrinsic luminosity. The Dupuy & Liu (2012) absolute K_s magnitude for an L0 dwarf is approximately 10.4. Allowing for the possibility of equal mass binarity we set our M_{Ks} lower limit at 9.7. The luminosity selection leaves us with 18 promising L0-T2 dwarf candidates, shown in Table D1 and Figure 14.

Since the fainter VVV L dwarfs will lack VIRAC parallax measurements (see Figure 11) but often have high proper motions, one might hope to identify additional brown dwarfs in a selection of high proper motion sources. Figure 15 illustrates this approach: the majority of sources with $\mu>30$ mas yr^{-1} that satisfy the above colour selection are reddened M dwarfs (i.e. relatively distant stars), whereas most of the subset with $\mu>100$ mas yr^{-1} are (probable) L dwarfs not subject to significant reddening because of their smaller distances. We take the above $Y-J$, $J-H$ and $H-K_s$ brown dwarf colour selection criteria and allow up to $A_V=1.5$ of reddening (Cardelli, Clayton & Mathis 1989) to define a brown dwarf selection region in the $Y-J$ vs. $J-H$ plane that is limited to a relatively narrow range of $J-H$ colours (see Figure 15). This will only select early type L dwarfs: later types are more difficult to distinguish from reddened M dwarfs and our intention is to make a reliable rather than complete selection of brown dwarfs. This yielded 66 early L dwarf candidates, see Table D2. The separation of these candidates from reddened M dwarfs is clearer in the $Z-J$ vs $J-H$ panel of Figure 15, for those candidates with a Z detection.

6.1.1 β Cir B

The young (∼ 400 Myr) L1-type age-benchmark companion to β Cir was discovered in a preliminary version of VIRAC (Smith et al. 2015) by a simple cross-match of L dwarf candidates against HIPPARCOS for stars with similar proper motion and parallax. It is included in Table D1 with the other L dwarf candidates identified by our colour, parallax and proper motion-based selection described above.

6.1.2 LTT 7251 B

LTT 7251 is a high proper motion G8 type dwarf at 37.6pc. It has been extensively studied and boasts a range of accurate chemical abundance measurements courtesy of the HARPS GTO planet search program (Adibekyan et al. 2012) and measurements of a number of other stellar parameters from the Geneva-Copenhagen Survey (Casagrande et al. 2011). Unfortunately, the current age estimates presented by the Geneva-Copenhagen Survey do not significantly constrain the age of LTT 7251 (approx. $1-10Gyr$). This could potentially be remedied with gyrochronology using a modestly sized telescope to observe this bright star ($V=8.54$, $K_s=6.7$).

We have identified a mid-late L dwarf common proper motion companion to LTT 7251 in the VIRAC proper motion data (LTT 7251 B henceforth) for which we obtained a near infrared spectrum with the ARCoIRIS spectrograph on the 4-m Blanco telescope (Figure 16) DETAILS NEEDED from Mariusz. This source did not fulfil the L dwarf selection criteria described in the previous section because it lacks Z and Y photometry in the standard VVV catalogue products of the CASU pipeline, owing to proximity to a diffraction spike associated with the much brighter primary and the slightly poorer spatial resolution of VISTA in the Z and Y passbands. The colour $J-H=0.57$ also failed our selection criterion, though this may simply be because of the significant uncertainty (0.14 mag). We were able to extract Z and Y photometry from the images by using a small photometric aperture and carefully placing a sky background aperture. Source magnitudes in a $1''$ diameter aperture are $K_s=15.5$, $H=16.36$, $J=16.93$ Insert ZY photometry and motions. The source also lacks a useful parallax measurement because

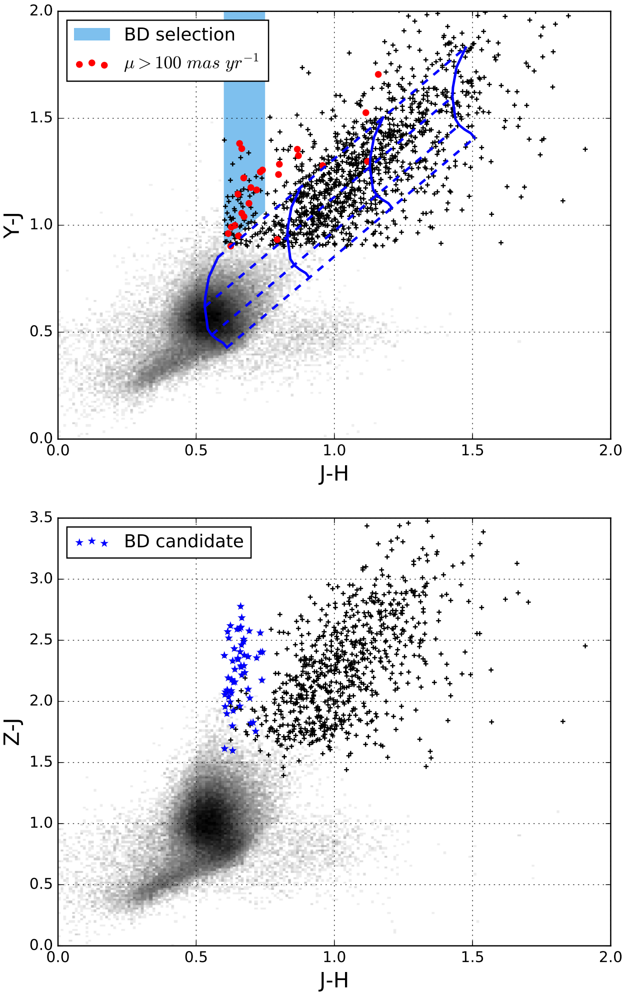

Figure 15. Density plots of $Y - J$ and $Z - J$ vs. $J - H$ for sources from VIRAC with YJHK detections, $\mu > 30$ mas yr^{-1}, σ_μ <5 mas yr^{-1} and flagged as 'reliable'. Overplotted in black pluses are those that meet the colour criteria for our brown dwarf selection in the parallax data. *upper*: In red are sources that have $\mu > 100$ mas yr^{-1}. Each solid lines shows the M dwarf subtype sequence (M0 bottom, M9 top) for a constant A_V, and each dashed line shows the reddening sequence for a constant M dwarf subtype at $A_V = 0$ (left) to $A_V = 9$ (right). The brown dwarf selection is explained in the text. *lower*: The M dwarfs are further from the early L dwarfs in $Z - J$ but we select on $Y - J$ since many objects are undetected in Z. The brown dwarf selection from the upper panel are shown as blue stars.

it is relatively faint. However, the probability of a chance projection of a high common proper motion companion at such a close separation is negligible.

A fit across the whole NIR spectrum gives an L4 spectral type (best fit template 2MASS J21580457-1550098, $\chi^2_{red} = 3.197$). However, the L4 template doesn't really reproduce the morphology of the J and K bands and the absolute magnitudes, $M_J = 14.05$, $M_H = 13.48$, $M_{Ks} = 12.6$, imply a later type. The L7-L9 templates give a much better fit to the shape of the spectrum, but the overall 1–2.5 μm slope is bluer (hence a larger χ^2) [CHECK THIS - NOT OBVIOUS in Fig.17].

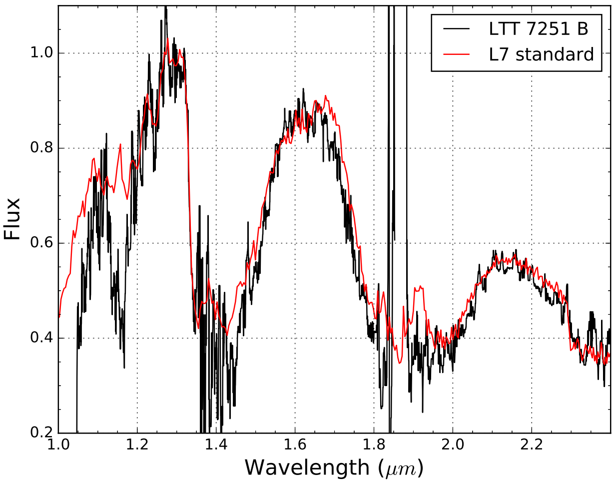

Figure 16. ARCoIRIS spectrum of LTT 7251 B plotted against the L7 optical standard DENIS-P J0205.4-1159 observed by Burgasser et al. (2010) and obtained from the SpeX prism library (Burgasser 2014).

If we fit the J, H, and K bands separately we obtain later spectral types:

J-band best fit: L5 SDSS J083506.16+195304.4 ($\chi^2_{red} = 2.3610$)
H-band best fit: L9 DENIS-P J0255-4700 ($\chi^2_{red} = 4.1937$)
K-band best fit: L6 2MASSI J1010148-040649 ($\chi^2_{red} = 2.6262$)

The average spectral type when fitting J, H, and K separately is L7, which agrees with the visual matching to the L7 spectral standard. It's mildly low metallicity is likely the explanation for the slightly blue colour of LTT 7251 B and the slight under-luminosity in the K_s band (~ 0.2 *mag*) relative to a field L7 dwarf.

The list of accurate chemical abundances available for LTT 7251 AB and potential for a reasonably accurate age determination via gyrochronology make the system a promising benchmark, a test of brown dwarf atmospheric forward grid models and retrieval methods (see e.g. Burningham et al. 2017).

6.1.3 2MASS J12564352-6202041

2MASS J12564352-6202041 (2MASS 1256-62 hereafter) is the only genuine source we identified through visual inspection of sources with $\mu > 1'' \, yr^{-1}$, and $10 < \sigma_\mu$ (mas yr^{-1}) < 30, see section 4.5.2. 2MASS 1256-62 is severely blended with a background source in the 2010 epochs; this is likely the cause of the relatively high uncertainty on the proper motion (hence epm flag=2 for both measurements). The pipeline proper motions for the source are -1112.08 ± 12.05 and -12.67 ± 16.29 mas yr^{-1} in $\alpha \cos\delta$ and δ respectively. The pipeline median K_s magnitude is 15.772 ± 0.036. Note that while we use robust methods where possible, pipeline outputs for this source are swayed to some extent by the blended early epochs. This source does not have a parallax in VIRAC, measurements were attempted in the two overlapping pawprint sets separately but they did not agree. To

α	12h56m41.63s	2012.0
δ	-62d02m03.93s	2012.0
$\mu_{\alpha \cos \delta}$	-1116.34 ± 4.12	mas yr^{-1}
μ_{δ}	3.91 ± 4.02	mas yr^{-1}
i	19.78 ± 0.06	mag
Z	17.86 ± 0.03	mag
Y	17.01 ± 0.02	mag
J	16.10 ± 0.01	mag
H	15.89 ± 0.02	mag
Ks	15.72 ± 0.03	mag

Table 1. Details of 2MASS 1256-62. All fluxes are on the Vega system

try to improve on the pipeline values with a more bespoke solution, we use all VVV K_s band observations of the source for a single fit, omitting those from the 2010 observing season. The median K_s band magnitude for these 82 epochs is 15.737 ± 0.056. Using astrometric reference sources this time drawn from within $1'$ radially about the target but an otherwise similar fitting procedure we measure proper motions of -1116.34 ± 4.12 and 3.91 ± 4.02 mas yr^{-1} in $\alpha \cos \delta$ and δ respectively and a parallax of 5.3 ± 7.1 mas. The ZYJH photometry that we have included in VIRAC are mostly taken from VVV DR4 at the VSA, corresponding to the first set of multi-filter data taken at the beginning of the survey. This source is blended with the background source in the early observations and hence shows null (99.999) ZYJH detections in VIRAC. We therefore obtained the ZYJHKs tile catalogue photometry produced from the second set of multi-filter observations made at the end of the survey. These magnitudes are given in Table 1. This field was also observed as part of the VPHAS+ survey, giving us an i band magnitude (also in Table 1) but non-detections in the r and $H\alpha$ observations. The source was detected in the J band in 2MASS (16.1 ± 0.1, photometric quality flag B), but not in the H and Ks bands (the upper limits on these magnitudes are 15.5 and 15.3 respectively).

2M1256-62 is a significant outlier from the locus of normal dwarf stars in Ks band reduced proper motion (see Figure 10). It has colours consistent with those of known L subdwarfs (Kirkpatrick et al. 2014; Zhang et al. 2017). On Zhang et al. (2017) figure 1 2M1256-62 would fall in the $T_{eff} = 2400 - 2500\ K$ range, of the $[Fe/H] \approx\ -1.0$ Bt Settl grids. This is promising evidence that 2M1256-62 is an esdL. Our FIRE spectrum is shown in Figure 17.

7 GALACTIC ROTATION CURVE

To demonstrate the usefulness of our catalogue out to large distances and across large areas we attempt to measure the galactic rotation curve tangential to the line of sight in the $l = 300^\circ$ direction using reasonably well calibrated red clump giant branch standard candles (López-Corredoira et al. 2002, Hawkins et al. 2017). We do this using VVV proper motion data at $299.5 < l < 300.5$ and $0.5 < |b| < 1.0$ with $10 < J < 20$ and $10 < Ks < 20$. On this sample we perform an approximate relative to absolute proper motion correction by using the median proper motion in Galactic longitude of a Besançon synthetic stellar population (Robin et al. 2003) in the direction of our VVV sample and at a Ks magnitude range identical to that of our astrometric reference source selection ($12.5 < Ks < 16.0$). We use a diffuse extinction parameter of 2.0 $mag\ kpc^{-1}$. Our relative to absolute corrections in μ_l at $l = 300^\circ$ are -6.0 mas yr^{-1} and -5.9 mas yr^{-1} for $b = 0.75$ and $b = -0.75$ respectively.

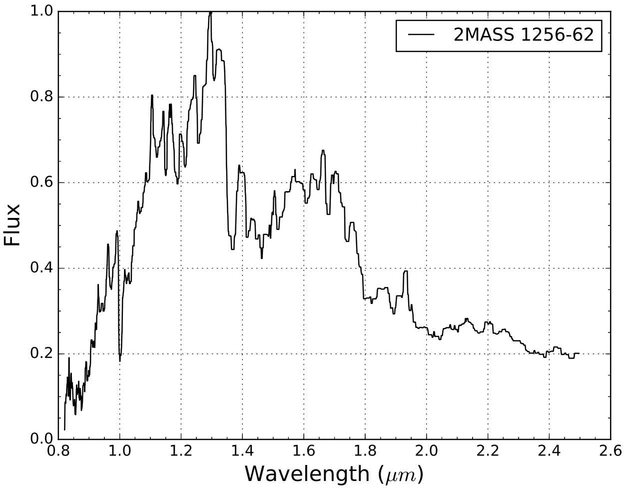

Figure 17. FIRE spectrum of 2MASS J12564352-6202041

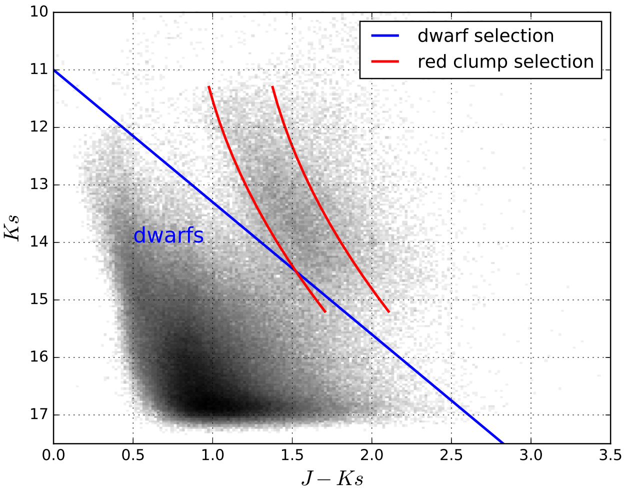

Figure 18. A log density plot of our $l = 300^\circ$ sample in $J - Ks$ vs. Ks colour magnitude space. Overplotted are our simple linear dwarf identification cutoff, and the ± 0.2 mag bounds around our fitted red clump giant tract that we use to select red clump giant stars.

We perform an initial approximate dwarf rejection for this Galactic coordinate range of $Ks > 2.3(J - Ks) + 11$ (see Figure 18). The remaining initial giant candidates in the range $11.3 < Ks < 15.5$ we split into 0.3 mag wide bins and find the approximate location of the peak of the $J - Ks$ distribution for each bin. Using a second order polynomial we fit the $J - Ks$ peak location to the median Ks magnitude for each bin to define our red clump giant tract. Sources with $J - Ks$ within 0.2 mag of this tract are our red clump giant selection (see Figure 18).

With our selected red clump giant branch we estimate

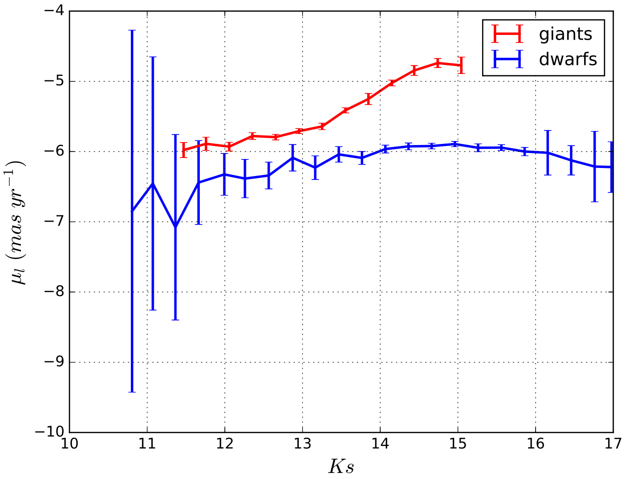

Figure 19. Binned Ks magnitudes and their median μ_l proper motion values for the dwarf and red clump giant selections shown in Figure 18.

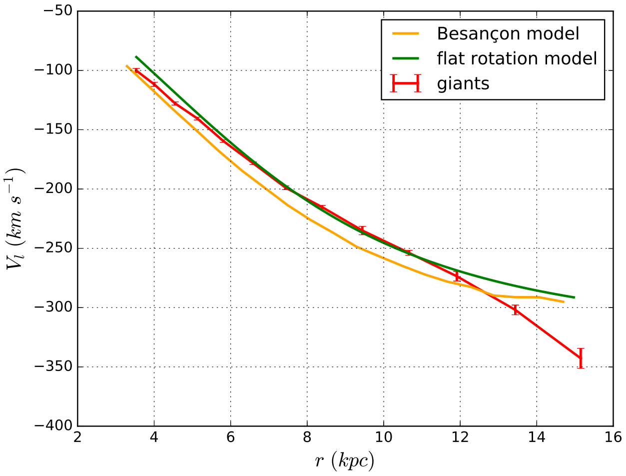

Figure 20. Tangential velocity in the l direction versus distance for our red clump giant selection, and the Besançon synthetic population and simple constant rotation model at the same $l = 300°$. The discrepancy at $r > 12$ *kpc* is likely to be due to a bias in selecting only the brightest red clump giants at the faint end of our sample.

distances using equations 8 and 9 of López-Corredoira et al. (2002), and the updated M_{Ks} and intrinsic $J - Ks$ colours of the red clump giants from Hawkins et al. (2017). We then measure the median μ_l and distance in each 0.3 *mag* wide Ks magnitude bin. Figure 19 shows the median μ_l vs. Ks magnitude and compares these to the equivalent for our earlier dwarf selection to show that we do indeed measure distinct proper motion distributions for each population. Note that the average motion for dwarfs in the $14 < Ks < 16$ range is approximately equal to the relative to absolute correction applied earlier, consistent with these comprising the bulk of our astrometric reference sources.

We then convert those median μ_l values to a median tangential velocity in l using the median distances for each bin and show the resulting velocity vs. distance curve in Figure 20. Also shown are the equivalent curves for the Besançon model acquired previously and for a simple model which assumes a flat rotation curve with $V_0 = 220$ $km\ s^{-1}$ and an 8.5 *kpc* galactocentric distance. The good agreement between our velocity curve and those of the models is encouraging, as are the uncertainty estimates on the velocities[3] (approx. 1.5 $km\ s^{-1}$ for $3.5 < d < 8.5$ kpc, and still below 5 $km\ s^{-1}$ at approx. 14 *kpc*). We note that our Besançon model-based relative to absolute correction is dominated by relatively nearby dwarf stars with $K_s \approx 15$–16 so this does not seriously compromise our comparison with the Besançon prediction for distant giants. We suspect that the turn down in our data which starts at around 12 *kpc* ($Ks \approx 14.5$ *mag*) is due to a bias toward detection of only the brighter giants, and probably also some contribution by the dwarfs. A push to slightly fainter magnitudes by using point spread function fitted astrometry/photometry would improve this.

7.1 Relative to Absolute Correction with Galaxies

That our Galactic rotation curve agrees reasonably well with the models suggests that our relative to absolute proper motion correction at $l = 300°$ based on average motions of the Besançon synthetic population was accurate. To investigate how well this approach might work at other Galactic locations, and to demonstrates the usefulness of VIRAC for investigating the space motions of populations inside the Galactic bulge, we compare proper motions of a Besançon synthetic model at the same magnitude range as the VIRAC astrometric reference sources ($12.5 < Ks < 16.0$) to those of VIRAC in tile b201 ($l = 350.8°$; $b = -9.7°$), one of the least dense fields in the VVV survey. Unlike in Section 7 (where we were sampling the inner disk) we are able to identify a population of external galaxies in tile b201 due to the relatively low stellar density (see Figure 4). We expect to still be able to select useful numbers of external galaxies at approximately $b = -3.5°$, less so closer to the equator. External galaxies should have negligible measurable absolute proper motion, and hence their average relative proper motion in VIRAC tells us the correction that must be applied to the relative motions of nearby (on the sky) objects to place them on an absolute frame (see e.g. Smith et al. 2014).

Figure 21 shows $J - Ks$ colour vs. Ks magnitude for VIRAC sources in tile b201 and the region inside which we select probable external galaxies. The contour shows the region inside which galaxy classifications accounted for 90% of sources that were classified in all bands as either stellar or galaxies. We also require our external galaxy selection to have no stellar modal classifications in any of their pawprint sets and galactic morphological classification in the ZYJH bands of VVV DR4. This selection yields 1,372 external galaxies.

The median and standard errors on the relative motions of the above selection were 1.15 ± 1.05 mas yr^{-1} and 4.79 ± 1.00 mas yr^{-1} in $\alpha \cos\delta$ and δ respectively.

---

[3] For the purpose of this demonstration we neglect to include the contribution of the distance uncertainty in the tangential velocity uncertainty.

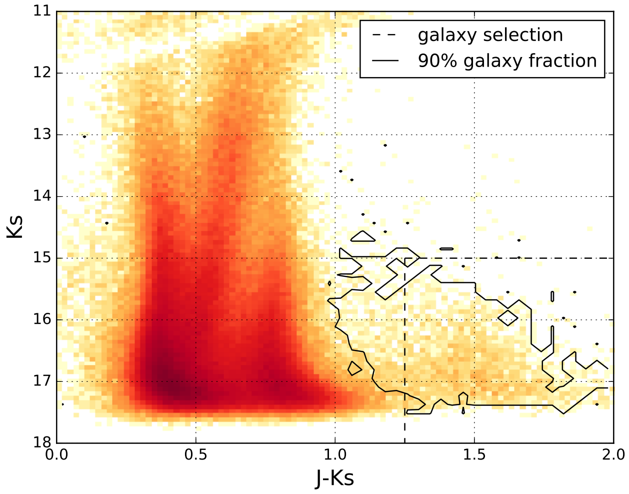

Figure 21. $J - Ks$ colour vs. Ks magnitude for tile b201, also shown is our colour-magnitude selection which when combined with a set of morphological classifications defines our external galaxy selection for this tile. The contour shows the region inside which galaxy classifications accounted for 90% of sources that were classified in all bands as either stellar or galaxies.

The average motions of sources in the Bescançon synthetic stellar population model at this Galactic location are -0.40 mas yr^{-1} and -2.41 mas yr^{-1} in $\alpha \cos\delta$ and δ respectively. Since we are comparing Besançon average absolute motions to the correction we would need to apply to convert VIRAC relative motions to absolute motions, the two should have equal magnitude and opposite sign. The values agree in $\mu_{\alpha\cos\delta}$, to within 0.7σ, but there is a significant (2.3σ) discrepancy between the two in μ_{delta}. Note that at this Galactic location $\mu_{\alpha\cos\delta} \approx \mu_b$ and $\mu_\delta \approx \mu_l$. Figure 22 shows the proper motion distributions in δ in more detail. The spread in the relative motions of the b201 galaxy selection is roughly consistent with their being at the faint end of VIRAC ($Ks > 14$); the significances of the external galaxies' proper motion deviations from zero after applying the 4.79 mas yr^{-1} relative to absolute correction in μ_{delta} are described well by a Gaussian distribution.

We have verified these results in the neighbouring VVV tile, b202 ($l = 352.2°$; $b = -9.7°$). The magnitude of the differences in $\mu_{\alpha\cos\delta}$ and μ_δ are the same but the significance of the differences are much lower (0.4 and 1.09 respectively) due to a wider spread in the relative proper motions of external galaxies in this tile.

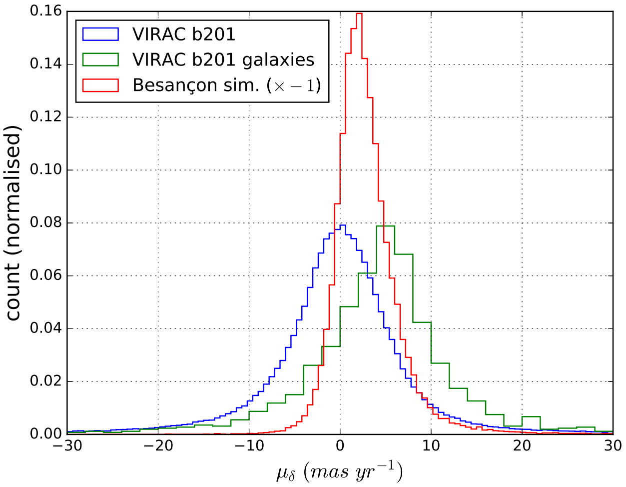

Figure 22. The distributions of VIRAC μ_δ for VVV tile b201 as a whole and a selection of external galaxies in tile b201 (see text). Also shown is the additive inverse of the absolute μ_δ of a Besançon synthetic stellar population at the same Galactic location. As expected, the average VIRAC relative motion of tile b201 as a whole is zero. The average relative motion of the selection of external galaxies, which should have effectively zero absolute motion, is 4.8 ± 1.0 mas yr^{-1}. The additive inverse of the average absolute motion of the Besançon stellar model should equal this value but it differs by $\approx 2.3\sigma$.

7.2 Other uses: Kinematic Distance Estimates and Cluster Decontamination

In principle, one can use proper motion to estimate distance to an object using a Galactic disc rotation model and assuming the source has a space velocity consistent with disk membership. This is routinely done with radial velocities (e.g. Contreras Peña et al. 2017). At minimum, proper motions can be used to provide useful constraints on source distances. E.g. VIRAC proper motion and parallax upper limits were used to determine that the very unusual long-duration transient source CX330 is outside the solar neighbourhood and moving too slowly to be connected to any known star forming complex (Britt et al. 2016), assuming an age of order 1 Myr. VIRAC kinematic distance estimates are most useful for objects known to be young and hence very likely to have space velocity consistent with disk rotation, these objects would include young objects (e.g. Cepheids) and open clusters.[ATTEMPT DISTANCE CONSTRAINT FOR CARLOS CONTRERAS YSOS THAT HAVE RADIAL VELOCITY DISTANCES.]

A further important use of VIRAC astrometry at large distances is kinematic decontamination of Galactic clusters. A good example of this was the case of the globular cluster FSR 1735 = 2MASS GC03 at $d = 11$ kpc (Carballo-Bello et al. 2016). They demonstrated that an early version of the VIRAC proper motions was able to reliably distinguish cluster members on the giant branch from field stars spread more equally across the dwarf and giant branches of the colour magnitude diagram, see figure 5 of that work.

8 SUMMARY

VIRAC V1 comprises 560 deg^2 of near-infrared proper motion and 5σ parallax catalogues of the southern Galactic plane and bulge comprising 312 million and 6,935 sources respectively. Sub-mas yr^{-1} precision on relative proper motions is typical for bright sources, and at the level of a few mas yr^{-1} at $K_s = 16$. Using separate astrometric measurements from overlapping sets of pawprints we have demonstrated that these uncertainties characterise the true statistical errors well. We present 18 L dwarf candidates with parallax measurements and a further 66 identified through their high proper motion. We have found one promising chemical abundance benchmark L dwarf and one L subdwarf with very blue colours and unusual spectral features.

Through measuring the Galactic rotation curve at $l = 300^\circ$ out to $d \approx 12$ kpc, we have demonstrated that VIRAC astrometry can be useful for objects at a large Galactic distance. We have identified some discrepancy between the absolute proper motions of Besançon synthetic stellar population and the equivalent measurement in VIRAC data in a part of the bulge that we checked for demonstration purposes ($l = 350.8^\circ$, $b = -9.7^\circ$). Due to the significant extinction in optical bandpasses in the Galactic mid-plane and bulge, VIRAC will continue to retain value in the era of Gaia and beyond.

ACKNOWLEDGMENTS

We acknowledge use of data from the ESO Public Survey programme ID 179.B-2002 taken with the VISTA telescope, data products from CASU, and funding from the FONDAP Center for Astrophysics 15010003, the BASAL CATA Center for Astrophysics and Associated Technologies PFB-06, the FONDECYT from CONICYT. LCS acknowledges a studentship funded by the Science & Technology Facilities Research Council (STFC) of the UK; PWL acknowledges the support of a consolidated grant (ST/J001333/1) also funded by STFC.

REFERENCES

Adibekyan V. Z., Sousa S. G., Santos N. C., Delgado Mena E., González Hernández J. I., Israelian G., Mayor M., Khachatryan G., 2012, A&A, 545, A32

Anglada-Escudé G. et al., 2016, Nature, 536, 437

Beamín J. C. et al., 2013, A&A, 557, L8

Britt C. T. et al., 2016, MNRAS, 460, 2822

Burgasser A. J., 2014, in Astronomical Society of India Conference Series, Vol. 11, Astronomical Society of India Conference Series

Burgasser A. J., Cruz K. L., Cushing M., Gelino C. R., Looper D. L., Faherty J. K., Kirkpatrick J. D., Reid I. N., 2010, ApJ, 710, 1142

Burningham B., Marley M. S., Line M. R., Lupu R., Visscher C., Morley C. V., Saumon D., Freedman R., 2017, ArXiv e-prints

Carballo-Bello J. A. et al., 2016, MNRAS, 462, 501

Cardelli J. A., Clayton G. C., Mathis J. S., 1989, ApJ, 345, 245

Casagrande L., Schönrich R., Asplund M., Cassisi S., Ramírez I., Meléndez J., Bensby T., Feltzing S., 2011, A&A, 530, A138

Chen Y., Seward F. D., Sun M., Li J.-t., 2008, ApJ, 676, 1040

Cioni M.-R. L. et al., 2016, A&A, 586, A77

Cioni M.-R. L. et al., 2014, A&A, 562, A32

Cirasuolo M. et al., 2014, in Proc. SPIE, Vol. 9147, Ground-based and Airborne Instrumentation for Astronomy V, p. 91470N

Contreras Peña C. et al., 2017, MNRAS, 465, 3039

Cross N. J. G. et al., 2012, A&A, 548, A119

Dalton G. et al., 2016, in Proc. SPIE, Vol. 9908, Ground-based and Airborne Instrumentation for Astronomy VI, p. 99081G

de Jong R. S. et al., 2016, in Proc. SPIE, Vol. 9908, Ground-based and Airborne Instrumentation for Astronomy VI, p. 99081O

Dupuy T. J., Liu M. C., 2012, ApJ, 201, 19

Gaia Collaboration et al., 2016, A&A, 595, A1

Hawkins K., Leistedt B., Bovy J., Hogg D. W., 2017, ArXiv e-prints

Ivanov V. D. et al., 2013, A&A, 560, A21

Kirkpatrick J. D. et al., 2014, ApJ, 783, 122

Kurtev R. et al., 2017, MNRAS, 464, 1247

Lewis J. R., Irwin M., Bunclark P., 2010, in Astronomical Society of the Pacific Conference Series, Vol. 434, Astronomical Data Analysis Software and Systems XIX, Mizumoto Y., Morita K.-I., Ohishi M., eds., p. 91

Libralato M. et al., 2015, MNRAS, 450, 1664

Lodieu N., Dobbie P. D., Deacon N. R., Hodgkin S. T., Hambly N. C., Jameson R. F., 2007, MNRAS, 380, 712

López-Corredoira M., Cabrera-Lavers A., Garzón F., Hammersley P. L., 2002, A&A, 394, 883

Lucas P. W. et al., 2008, MNRAS, 391, 136

Lutz T. E., Kelker D. H., 1973, PASP, 85, 573

Majewski S. R., APOGEE Team, APOGEE-2 Team, 2016, Astronomische Nachrichten, 337, 863

Majewski S. R. et al., 2015, ArXiv e-prints

Michalik D., Lindegren L., Hobbs D., 2015, A&A, 574, A115

Minniti D. et al., 2010, NewA, 15, 433

Robin A. C., Reylé C., Derrière S., Picaud S., 2003, A&A, 409, 523

Rojas-Ayala B., Iglesias D., Minniti D., Saito R. K., Surot F., 2014, A&A, 571, A36

Skrutskie M. F. et al., 2006, AJ, 131, 1163

Smith L., Lucas P. W., Burningham B., Jones H. R. A., Smart R. L., Andrei A. H., Catalán S., Pinfield D. J., 2014, MNRAS, 437, 3603

Smith L. C. et al., 2015, MNRAS, 454, 4476

Sutherland W. et al., 2015, A&A, 575, A25

Taylor M. B., 2005, in Astronomical Society of the Pacific Conference Series, Vol. 347, Astronomical Data Analysis Software and Systems XIV, Shopbell P., Britton M., Ebert R., eds., p. 29

Taylor M. B., 2006, in Astronomical Society of the Pacific Conference Series, Vol. 351, Astronomical Data Analysis Software and Systems XV, Gabriel C., Arviset C., Ponz D., Enrique S., eds., p. 666

Torres C. A. O., Quast G. R., da Silva L., de La Reza R., Melo C. H. F., Sterzik M., 2006, A&A, 460, 695

van Leeuwen F., 2007, A&A, 474, 653

Zhang Z. H. et al., 2017, MNRAS, 464, 3040

APPENDIX A: CONFIRMED HPM SOURCES

APPENDIX B: PARALLAX SOURCES

APPENDIX C: TGAS CPM SOURCES

APPENDIX D: L DWARF CANDIDATES

#	$\alpha_{2012.0}$	$\delta_{2012.0}$	$\mu_{\alpha\cos\delta}$	μ_δ	Z	Y	J	H	Ks
1	11h38m53.05s	-63d46m04.54s	−486.45 ± 0.88	9.72 ± 0.77	13.27 ± 0.01	12.71 ± 0.01	11.71 ± 0.01	11.39 ± 0.01	11.35 ± 0.01
2	11h39m17.78s	-63d00m41.58s	−211.71 ± 0.83	122.61 ± 0.74	14.62 ± 0.01	14.01 ± 0.01	13.38 ± 0.01	13.06 ± 0.01	12.69 ± 0.02
3	11h41m44.65s	-63d28m26.79s	−224.34 ± 0.88	109.19 ± 0.78	12.91 ± 0.01	12.57 ± 0.01	12.40 ± 0.01	12.56 ± 0.01	11.30 ± 0.07
4	11h46m27.36s	-60d36m40.41s	−23.34 ± 2.19	−219.78 ± 2.23	11.75 ± 0.01	11.26 ± 0.01	10.62 ± 0.01	10.30 ± 0.01	10.10 ± 0.07
5	11h51m51.42s	-59d57m29.86s	−23.97 ± 0.89	266.86 ± 0.87	14.49 ± 0.01	13.80 ± 0.01	13.18 ± 0.01	12.42 ± 0.01	12.46 ± 0.01
6	11h53m04.81s	-62d01m44.55s	−262.73 ± 0.75	10.02 ± 0.81	13.70 ± 0.01	13.06 ± 0.01	12.39 ± 0.01	11.48 ± 0.01	11.59 ± 0.01
7	11h54m03.86s	-60d05m29.35s	−565.55 ± 0.85	216.76 ± 0.83	13.63 ± 0.01	12.99 ± 0.01	12.37 ± 0.01	11.62 ± 0.01	11.64 ± 0.01
8	11h54m21.72s	-63d14m27.22s	346.28 ± 0.92	−179.57 ± 0.92	*nan* ± *nan*	13.12 ± 0.01	12.50 ± 0.01	12.99 ± 0.01	11.72 ± 0.01
9	11h54m33.99s	-61d50m50.21s	−248.61 ± 1.13	86.91 ± 1.03	13.15 ± 0.01	12.13 ± 0.01	11.53 ± 0.01	11.08 ± 0.01	11.15 ± 0.01
10	11h54m52.81s	-62d39m17.56s	−740.64 ± 1.81	142.85 ± 1.80	15.75 ± 0.01	15.52 ± 0.01	15.11 ± 0.01	14.89 ± 0.01	14.87 ± 0.01

Table A1. High proper motion sources confirmed by visual inspection. *Full table in online data.*

#	$\alpha_{2012.0}$	$\delta_{2012.0}$	$\mu_{\alpha\cos\delta}$	μ_δ	π	Z	Y	J	H	Ks
1	11h38m53.06s	-63d46m04.54s	−482.00 ± 0.70	13.14 ± 0.71	16.9 ± 1.7	13.27 ± 0.01	12.71 ± 0.01	11.71 ± 0.01	11.39 ± 0.01	11.35 ± 0.
2	11h39m15.84s	-63d03m36.99s	−115.79 ± 0.77	30.45 ± 0.72	15.2 ± 1.7	15.62 ± 0.01	14.67 ± 0.01	13.77 ± 0.01	13.20 ± 0.01	12.75 ± 0.
3	11h39m17.78s	-63d00m41.58s	−210.52 ± 0.65	121.91 ± 0.72	14.6 ± 1.6	14.62 ± 0.01	14.01 ± 0.01	13.38 ± 0.01	13.06 ± 0.01	12.69 ± 0.
4	11h39m21.52s	-63d29m02.18s	−140.25 ± 0.49	16.96 ± 0.58	16.3 ± 1.3	13.54 ± 0.01	13.04 ± 0.01	12.10 ± 0.01	11.67 ± 0.01	11.68 ± 0.
5	11h40m08.73s	-62d32m43.31s	−158.83 ± 0.68	45.83 ± 0.89	11.3 ± 1.8	13.24 ± 0.01	12.73 ± 0.01	11.72 ± 0.01	11.34 ± 0.01	11.32 ± 0.
6	11h40m34.75s	-63d14m04.92s	−71.43 ± 0.60	11.48 ± 0.60	8.2 ± 1.4	13.97 ± 0.01	13.43 ± 0.01	12.81 ± 0.01	100.00 ± 100.00	11.97 ± 0.
7	11h40m43.80s	-63d14m41.62s	25.90 ± 0.75	43.91 ± 0.77	10.2 ± 1.8	16.36 ± 0.01	15.63 ± 0.01	14.86 ± 0.01	14.34 ± 0.01	13.96 ± 0.
8	11h41m01.50s	-62d15m44.79s	−97.91 ± 0.82	10.42 ± 0.72	10.6 ± 1.8	13.15 ± 0.01	12.68 ± 0.01	11.69 ± 0.01	100.00 ± 100.00	11.35 ± 0.
9	11h43m52.81s	-61d46m07.19s	−35.55 ± 0.62	3.00 ± 0.61	10.3 ± 1.9	13.79 ± 0.01	13.32 ± 0.01	12.76 ± 0.01	11.83 ± 0.01	11.96 ± 0.
10	11h43m56.82s	-62d07m57.01s	−49.12 ± 0.61	15.58 ± 0.62	9.2 ± 1.4	15.51 ± 0.01	14.90 ± 0.01	14.26 ± 0.01	13.76 ± 0.01	13.43 ± 0.

Table B1. Parallax sources measured at 5σ *Full table in online data.*

Name	$\alpha_{2015.0}$	$\delta_{2015.0}$	$\mu_{\alpha\cos\delta}$	μ_δ	π	Gaia g Mag	Ks	MKs	ρ	$\rho(au)$
HD 147436 A	16h24m13.46s	-47d35m16.3s	−79.02 ± 0.11	−72.57 ± 0.07	16.71 ± 0.24	9.04	7.51 ± 0.02	3.62		
HD 147436 B	16h24m13.24s	-47d35m15.4s	−75.72 ± 2.83	−74.59 ± 2.82			11.12 ± 0.02	7.24	2.4	143
TYC 8990-1546-1 A	13h17m50.13s	-60d41m11.1s	151.11 ± 0.59	−51.80 ± 0.77	22.44 ± 0.26	9.74	7.51 ± 0.03	4.26		
TYC 8990-1546-1 B	13h17m50.44s	-60d41m13.0s	156.11 ± 1.64	−47.35 ± 1.81			10.02 ± 0.10	6.78	3.0	135
TYC 8975-2832-1 A	12h24m39.97s	-61d23m21.5s	−116.11 ± 0.72	−27.73 ± 1.14	6.18 ± 0.33	9.72	7.98 ± 0.02	1.93		
TYC 8975-2832-1 B	12h24m39.79s	-61d23m18.6s	−112.56 ± 1.27	−35.29 ± 1.69			12.47 ± 0.02	6.42	3.1	503
TYC 8691-2744-1 A	14h27m27.87s	-59d12m33.3s	−74.52 ± 1.07	−108.75 ± 0.45	8.89 ± 0.23	11.64	9.53 ± 0.03	4.27		
TYC 8691-2744-1 B	14h27m28.04s	-59d12m30.8s	−70.66 ± 1.58	−109.65 ± 1.56			10.79 ± 0.10	5.53	2.9	323
TYC 7365-318-1 A	17h12m16.50s	-32d16m32.9s	92.77 ± 1.69	−93.60 ± 1.25	11.12 ± 0.22	10.36	8.73 ± 0.03	3.96		
TYC 7365-318-1 B	17h12m16.73s	-32d16m30.9s	96.03 ± 0.69	−95.30 ± 0.74			11.61 ± 0.01	6.84	3.6	320
HD 160460 A	17h41m02.82s	-24d51m54.2s	36.75 ± 2.03	−127.34 ± 1.84	8.93 ± 0.22	9.92	8.48 ± 0.05	3.23		
HD 160460 B	17h41m02.64s	-24d51m52.0s	44.81 ± 1.21	−119.60 ± 1.04			13.04 ± 0.02	7.79	3.3	371
HD 124787 A	14h17m26.36s	-58d52m38.4s	−76.73 ± 1.35	−160.34 ± 0.51	13.38 ± 0.27	9.81	8.15 ± 0.02	3.78		
HD 124787 B	14h17m26.36s	-58d52m35.2s	−68.79 ± 2.87	−160.66 ± 2.70			11.73 ± 0.02	7.36	3.2	238
HD 158940 A	17h33m00.33s	-24d19m25.3s	−18.99 ± 0.09	−115.99 ± 0.04	10.31 ± 0.31	8.34	7.36 ± 0.03	2.43		
HD 158940 B	17h33m00.58s	-24d19m26.9s	−20.92 ± 1.29	−109.39 ± 1.03			12.05 ± 0.02	7.12	3.7	363
CD-60 5315 A	14h45m58.27s	-61d30m10.6s	−117.76 ± 1.68	−16.35 ± 0.65	2.77 ± 0.32	9.78				
CD-60 5315 B	14h45m58.65s	-61d30m13.4s	−107.88 ± 5.06	−22.86 ± 5.81			13.04 ± 0.03	5.25	3.9	1402
TYC 6861-2092-1 A	18h32m53.32s	-25d30m53.9s	35.78 ± 1.91	−113.74 ± 1.88	5.85 ± 0.22	10.96	9.34 ± 0.03	3.18		
TYC 6861-2092-1 B	18h32m53.03s	-25d30m52.8s	36.31 ± 0.68	−106.49 ± 0.55			13.27 ± 0.01	7.11	4.1	708
TYC 7365-627-1 A	17h10m48.64s	-33d14m28.0s	31.76 ± 1.95	−114.39 ± 1.51	6.95 ± 0.25	11.22	9.67 ± 0.03	3.88		
TYC 7365-627-1 B	17h10m48.53s	-33d14m23.2s	33.30 ± 0.76	−111.98 ± 0.70			12.67 ± 0.01	6.88	5.0	723
HD 166745 A	18h13m33.07s	-33d30m00.2s	−135.60 ± 0.12	−235.33 ± 0.08	16.30 ± 0.23	8.28	6.82 ± 0.03	2.88		
HD 166745 B	18h13m32.56s	-33d29m57.9s	−126.89 ± 1.06	−230.39 ± 0.96			12.29 ± 0.01	8.35	6.8	416
HD 132401 A	15h01m35.38s	-59d38m43.8s	−120.21 ± 0.08	−236.99 ± 0.07	15.12 ± 0.34	8.9	7.25 ± 0.02	3.15		
HD 132401 B	15h01m35.14s	-59d38m52.5s	−117.98 ± 1.06	−234.85 ± 1.23			13.40 ± 0.01	9.30	8.8	585
HD 130265 A	14h49m31.35s	-59d07m55.3s	−130.17 ± 0.09	−50.51 ± 0.07	20.74 ± 0.22	8.31	6.79 ± 0.02	3.37		
HD 130265 B	14h49m32.39s	-59d07m52.8s	−120.93 ± 2.08	−56.67 ± 2.26			11.26 ± 0.01	7.85	8.4	404
TYC 8703-265-1 A	15h30m20.91s	-57d52m21.2s	−36.93 ± 1.21	−115.38 ± 0.59	7.36 ± 0.25	11.19	9.31 ± 0.02	3.64		
TYC 8703-265-1 B	15h30m19.75s	-57d52m16.7s	−28.21 ± 1.42	−111.52 ± 1.54			11.09 ± 0.05	5.43	10.3	1396
CD-53 6250 A	15h48m38.82s	-53d40m45.1s	−80.71 ± 1.37	−176.52 ± 0.42	8.88 ± 0.32	10.45	8.86 ± 0.02	3.60		
CD-53 6250 B	15h48m40.13s	-53d40m46.0s	−75.52 ± 1.80	−175.24 ± 1.78			10.52 ± 0.04	5.27	11.7	1313
L 149-77 A	14h12m28.43s	-62d56m12.1s	162.33 ± 0.47	191.87 ± 0.89	18.94 ± 0.34	10.58	8.22 ± 0.02	4.61		
L 149-77 B	14h12m29.20s	-62d56m25.0s	175.18 ± 1.21	188.17 ± 1.28			10.20 ± 0.04	6.59	13.9	735
LTT 7251 A	18h15m49.14s	-23d48m59.9s	64.83 ± 0.08	−166.27 ± 0.05	26.59 ± 0.31	8.3	6.73 ± 0.03	3.85		
LTT 7251 B	18h15m49.14s	-23d48m45.2s	76.30 ± 6.93	−172.01 ± 5.13			15.47 ± 0.05	12.6	14.7	552
L 200-41 A	15h18m40.13s	-56d27m58.0s	−174.73 ± 3.28	−143.07 ± 0.78	7.82 ± 0.66	11.33	9.57 ± 0.03	4.04		
L 200-41 B	15h18m39.64s	-56d28m15.2s	−169.25 ± 1.27	−139.88 ± 1.28			10.19 ± 0.04	4.65	17.7	2258
TYC 7869-41-1 A	17h09m52.74s	-39d22m30.8s	4.26 ± 1.73	−100.14 ± 1.38	6.74 ± 0.28	11.6	9.56 ± 0.03	3.70		
TYC 7869-41-1 B	17h09m52.70s	-39d22m11.4s	6.51 ± 0.99	−96.50 ± 1.07			10.19 ± 0.04	4.34	19.5	2884
CD-29 13392 A	17h19m50.46s	-30d01m49.9s	−118.88 ± 1.50	−48.53 ± 1.24	6.17 ± 0.35	9.89	8.34 ± 0.03	2.29		
CD-29 13392 B	17h19m48.99s	-30d01m43.2s	−118.45 ± 0.54	−44.96 ± 0.54			13.10 ± 0.01	7.05	20.3	3297
TYC 7899-2231-1 A	18h09m52.50s	-38d37m55.8s	11.22 ± 3.54	−145.99 ± 3.44	5.32 ± 0.27	11.59	10.04 ± 0.02	3.67		
TYC 7899-2231-1 B	18h09m50.23s	-38d37m51.8s	12.30 ± 0.59	−140.52 ± 0.58			12.14 ± 0.01	5.77	26.9	5050
TYC 7403-5878-1 A	18h03m24.14s	-37d07m07.9s	−39.98 ± 1.88	−114.24 ± 1.87	6.48 ± 0.26	11.51	9.73 ± 0.02	3.79		
TYC 7403-5878-1 B	18h03m25.12s	-37d06m35.9s	−40.52 ± 0.90	−111.50 ± 0.94			11.14 ± 0.02	5.20	34.1	5268
HD 134162 A	15h10m57.57s	-58d44m58.5s	−24.09 ± 1.00	−104.65 ± 0.56	11.74 ± 0.26	9.8	8.23 ± 0.03	3.58		
HD 134162 B	15h10m53.21s	-58d44m32.2s	−18.04 ± 1.29	−101.32 ± 1.36			12.57 ± 0.00	7.92	43.0	3661
HD 330817 A	16h26m06.59s	-48d30m01.7s	−149.33 ± 0.79	4.63 ± 1.69	11.31 ± 0.54	9.98	8.49 ± 0.02	3.76		
HD 330817 B	16h26m06.09s	-48d29m16.3s	−145 ± 0.76	7.44 ± 0.76			12.34 ± 0.01	7.61	45.7	4040
TYC 8982-1530-1 A	12h10m51.52s	-64d25m28.3s	−116.45 ± 0.84	−45.93 ± 0.58	15.69 ± 0.32	9.41	7.77 ± 0.03	3.75		
TYC 8982-1530-1 B	12h10m50.03s	-64d24m43.7s	−110.14 ± 0.79	−47.02 ± 0.74			12.20 ± 0.01	8.18	45.7	2911
HD 312272 A	13h01m43.91s	-62d10m13.3s	−97.48 ± 0.79	−55.25 ± 1.13	9.18 ± 0.29	9.83				
HD 312272 B	13h01m52.12s	-62d10m26.9s	−87.96 ± 0.92	−59.10 ± 0.99			10.54 ± 0.03	5.35	59.1	6438
TYC 8702-11-1 A	15h15m03.07s	-58d03m07.9s	−152.71 ± 1.12	−107.23 ± 0.28	8.23 ± 0.27	10.43	8.82 ± 0.02	3.40		
TYC 8702-11-1 B	15h15m11.32s	-58d02m58.2s	−148.55 ± 0.62	−106.60 ± 0.58			12.18 ± 0.01	6.76	66.2	8043

Table C1. VVV common proper motion companions to TGAS high proper motion sources.

#	$\alpha_{2012.0}$	$\delta_{2012.0}$	$\mu_{\alpha \cos \delta}$	μ_{δ}	π	Z	Y	J	H	Ks	
1	12h27m08.17s	-62d14m20.07s	−29.61 ± 0.83	−11.73 ± 0.71	14.03 ± 2.19	17.92 ± 0.02	16.75 ± 0.01	15.76 ± 0.01	15.13 ± 0.01	14.53 ± 0.01	10.2
2	13h26m57.62s	-61d18m18.13s	−199.38 ± 0.62	−64.37 ± 0.71	15.17 ± 1.53	17.03 ± 0.01	15.97 ± 0.01	15.07 ± 0.01	14.44 ± 0.01	13.96 ± 0.01	9.8
3	13h36m47.45s	-61d46m48.48s	129.02 ± 0.85	55.86 ± 0.93	30.95 ± 1.89	18.49 ± 0.03	17.21 ± 0.02	15.93 ± 0.01	15.13 ± 0.01	14.55 ± 0.01	12.0
4	14h01m16.88s	-60d55m53.74s	−121.15 ± 1.49	−131.96 ± 1.62	30.90 ± 3.37	20.49 ± 0.12	18.90 ± 0.06	17.20 ± 0.03	16.04 ± 0.02	15.05 ± 0.02	12.5
5	14h07m05.64s	-62d46m55.76s	−144.46 ± 1.85	−121.93 ± 1.60	30.39 ± 3.73	19.43 ± 0.07	18.16 ± 0.04	16.84 ± 0.02	15.97 ± 0.02	15.38 ± 0.03	12.8
6	15h03m59.87s	-60d28m14.37s	22.77 ± 0.95	−5.41 ± 1.20	13.78 ± 2.08	18.02 ± 0.03	16.92 ± 0.02	15.82 ± 0.01	15.15 ± 0.01	14.60 ± 0.01	10.3
7	15h17m21.47s	-58d51m31.36s	−91.17 ± 0.67	−127.80 ± 0.86	34.39 ± 1.60	16.73 ± 0.01	15.59 ± 0.01	14.44 ± 0.01	13.73 ± 0.01	13.18 ± 0.01	10.8
8	16h18m02.54s	-50d48m41.96s	−58.41 ± 1.08	−152.10 ± 1.45	19.55 ± 2.28	no detection	17.95 ± 0.05	16.59 ± 0.03	15.73 ± 0.02	15.07 ± 0.01	11.5
9	16h39m53.35s	-48d04m40.59s	40.91 ± 1.03	−26.63 ± 1.17	20.68 ± 2.02	18.04 ± 0.02	16.84 ± 0.01	15.45 ± 0.01	14.67 ± 0.01	14.02 ± 0.02	10.5
10	17h01m47.44s	-41d14m55.46s	−3.91 ± 1.05	−28.76 ± 1.16	14.90 ± 2.56	18.67 ± 0.03	17.40 ± 0.02	16.28 ± 0.01	15.54 ± 0.01	14.86 ± 0.01	10.7
11	17h03m42.52s	-34d42m48.01s	−29.71 ± 0.65	−103.55 ± 0.68	24.70 ± 1.45	16.13 ± 0.01	15.03 ± 0.01	14.04 ± 0.01	13.41 ± 0.01	12.93 ± 0.01	9.8
12	17h44m36.21s	-35d34m41.11s	−64.38 ± 0.82	−40.17 ± 0.81	12.84 ± 1.56	18.02 ± 0.10	16.84 ± 0.06	15.85 ± 0.04	15.23 ± 0.04	14.73 ± 0.01	10.2
13	17h52m28.62s	-39d52m59.73s	14.51 ± 1.15	−267.92 ± 1.09	10.34 ± 1.91	no coverage	17.70 ± 0.08	16.43 ± 0.02	15.76 ± 0.03	15.32 ± 0.02	10.3
14	18h08m04.69s	-30d49m48.20s	6.09 ± 1.29	−159.04 ± 1.25	17.09 ± 2.21	18.42 ± 0.15	17.21 ± 0.07	16.07 ± 0.04	15.42 ± 0.03	14.95 ± 0.02	11.1
15	18h12m51.63s	-31d04m50.84s	110.57 ± 0.68	−69.67 ± 0.63	29.18 ± 1.31	15.97 ± 0.01	14.86 ± 0.01	13.91 ± 0.01	13.22 ± 0.01	12.73 ± 0.01	10.0
16	18h26m33.50s	-33d41m38.14s	−45.58 ± 0.56	−93.87 ± 0.60	19.71 ± 0.90	17.09 ± 0.01	15.89 ± 0.01	14.73 ± 0.01	14.01 ± 0.01	13.42 ± 0.01	9.8
17	18h32m23.59s	-28d31m04.86s	17.40 ± 0.78	9.86 ± 0.79	12.97 ± 1.38	17.38 ± 0.03	16.25 ± 0.01	15.29 ± 0.01	14.65 ± 0.01	14.21 ± 0.01	9.7
18	18h34m17.26s	-27d54m07.62s	7.57 ± 0.59	−138.10 ± 0.68	28.66 ± 1.05	15.82 ± 0.01	14.58 ± 0.01	13.62 ± 0.01	13.01 ± 0.01	12.51 ± 0.01	9.7

Table D1. L0-T2 dwarf candidates from our parallax catalogue based on NIR colours and Ks band luminosity.

#	$\alpha_{2012.0}$	$\delta_{2012.0}$	$\mu_{\alpha \cos \delta}$	μ_{δ}	Z	Y	J	H	Ks
1	12h07m52.19s	-63d07m31.76s	−14.21 ± 1.69	−54.81 ± 1.72	18.14 ± 0.03	17.11 ± 0.02	16.18 ± 0.01	15.58 ± 0.01	15.11 ± 0.02
2	12h08m19.98s	-60d38m00.38s	49.26 ± 1.50	−33.90 ± 2.14	18.39 ± 0.03	17.60 ± 0.03	16.56 ± 0.01	15.85 ± 0.01	15.35 ± 0.03
3	12h16m44.53s	-60d47m45.95s	−31.26 ± 0.86	−9.20 ± 0.78	17.61 ± 0.02	16.26 ± 0.01	15.18 ± 0.01	14.54 ± 0.01	13.94 ± 0.01
4	12h21m09.82s	-62d14m40.77s	−32.95 ± 1.43	−16.40 ± 1.88	18.85 ± 0.04	17.44 ± 0.02	16.23 ± 0.01	15.61 ± 0.01	15.08 ± 0.02
5	12h27m08.16s	-62d14m20.07s	−30.36 ± 0.93	−11.78 ± 0.74	17.92 ± 0.02	16.75 ± 0.01	15.76 ± 0.01	15.13 ± 0.01	14.53 ± 0.01
6	12h31m31.06s	-62d26m31.71s	−32.81 ± 1.10	−12.97 ± 1.02	18.21 ± 0.03	16.77 ± 0.01	15.63 ± 0.01	15.02 ± 0.01	14.44 ± 0.01
7	12h50m03.57s	-61d53m51.73s	−54.69 ± 1.88	−18.14 ± 1.51	19.07 ± 0.04	17.83 ± 0.03	16.67 ± 0.01	15.93 ± 0.02	15.35 ± 0.02
8	12h50m58.04s	-64d06m53.26s	−64.21 ± 2.34	7.04 ± 3.00	18.87 ± 0.05	17.65 ± 0.03	16.69 ± 0.02	16.06 ± 0.02	15.61 ± 0.03
9	13h01m54.89s	-61d12m58.33s	−27.02 ± 0.67	−14.39 ± 0.65	17.30 ± 0.01	16.02 ± 0.01	15.02 ± 0.01	14.36 ± 0.01	13.77 ± 0.01
10	13h02m45.67s	-60d49m11.64s	50.16 ± 1.85	−17.00 ± 1.87	18.73 ± 0.04	17.84 ± 0.03	16.80 ± 0.02	16.17 ± 0.01	15.72 ± 0.03
11	13h09m45.07s	-62d08m25.40s	−314.60 ± 2.52	37.45 ± 1.82	19.55 ± 0.08	18.23 ± 0.05	16.87 ± 0.02	16.20 ± 0.02	15.60 ± 0.03
12	13h10m37.35s	-63d25m31.33s	−30.70 ± 1.82	−14.53 ± 1.87	18.78 ± 0.04	17.38 ± 0.02	16.26 ± 0.01	15.65 ± 0.01	15.08 ± 0.02
13	13h14m19.21s	-63d03m12.83s	−131.93 ± 1.35	−4.50 ± 1.22	18.17 ± 0.02	17.01 ± 0.01	15.95 ± 0.01	15.29 ± 0.01	14.80 ± 0.01
14	13h22m16.53s	-61d24m03.55s	−27.37 ± 2.29	−18.68 ± 2.01	19.44 ± 0.09	18.00 ± 0.04	16.84 ± 0.02	16.20 ± 0.02	15.74 ± 0.03
15	13h37m32.74s	-63d16m20.83s	−27.86 ± 2.07	−19.77 ± 2.11	18.01 ± 0.02	16.67 ± 0.01	15.50 ± 0.01	14.83 ± 0.01	14.26 ± 0.02
16	13h48m32.16s	-59d57m32.48s	−174.47 ± 2.13	−61.32 ± 2.18	19.02 ± 0.04	17.86 ± 0.03	16.86 ± 0.02	16.22 ± 0.02	15.76 ± 0.03
17	14h07m15.97s	-61d37m34.30s	−25.15 ± 0.94	−21.26 ± 1.09	18.48 ± 0.02	17.01 ± 0.01	15.87 ± 0.01	15.21 ± 0.01	14.58 ± 0.01
18	14h12m25.39s	-60d19m41.10s	−17.20 ± 1.15	−63.83 ± 1.38	17.52 ± 0.01	16.44 ± 0.01	15.48 ± 0.01	14.87 ± 0.01	14.37 ± 0.01
19	14h22m26.91s	-59d18m30.89s	−48.00 ± 1.74	−40.15 ± 1.67	19.04 ± 0.05	17.81 ± 0.03	16.70 ± 0.02	16.04 ± 0.02	15.52 ± 0.02
20	14h58m00.49s	-57d08m35.34s	−51.75 ± 2.23	−77.20 ± 2.02	19.30 ± 0.08	18.10 ± 0.06	16.94 ± 0.02	16.25 ± 0.03	15.75 ± 0.02
21	15h14m00.79s	-57d38m40.12s	−34.70 ± 5.35	29.19 ± 7.70	19.04 ± 0.06	18.08 ± 0.04	16.86 ± 0.02	16.13 ± 0.03	15.68 ± 0.04
22	15h16m13.37s	-58d36m27.61s	−31.04 ± 5.53	11.01 ± 5.52	no detection	18.51 ± 0.05	17.36 ± 0.03	16.65 ± 0.04	15.76 ± 0.03
23	15h16m21.44s	-55d24m35.34s	−67.68 ± 1.39	25.02 ± 1.45	17.90 ± 0.03	16.92 ± 0.02	16.00 ± 0.01	15.39 ± 0.01	14.93 ± 0.02
24	15h25m58.50s	-57d03m06.40s	−20.81 ± 2.34	−29.61 ± 2.29	18.80 ± 0.04	17.70 ± 0.03	16.74 ± 0.02	16.14 ± 0.03	15.62 ± 0.03
25	15h32m35.50s	-56d49m30.75s	−39.82 ± 2.92	−47.77 ± 3.15	18.91 ± 0.04	17.72 ± 0.03	16.65 ± 0.02	16.01 ± 0.02	15.55 ± 0.02
26	15h32m43.03s	-57d52m39.56s	−4.81 ± 3.06	−77.68 ± 3.19	18.87 ± 0.05	17.78 ± 0.03	16.77 ± 0.02	16.08 ± 0.03	15.58 ± 0.03
27	15h42m06.55s	-57d25m29.69s	−21.56 ± 1.79	−28.38 ± 1.63	18.84 ± 0.05	17.65 ± 0.03	16.55 ± 0.02	15.89 ± 0.03	15.38 ± 0.02
28	15h56m45.65s	-56d09m37.04s	−17.88 ± 2.06	−45.02 ± 2.03	19.40 ± 0.14	18.13 ± 0.08	17.00 ± 0.04	16.34 ± 0.04	15.88 ± 0.04
29	15h59m46.56s	-55d50m39.38s	−96.93 ± 1.48	−97.40 ± 1.46	19.14 ± 0.12	17.93 ± 0.07	16.54 ± 0.03	15.89 ± 0.03	15.34 ± 0.02
30	16h09m01.77s	-52d41m34.90s	−18.85 ± 5.25	−24.95 ± 4.88	18.93 ± 0.05	17.58 ± 0.03	16.55 ± 0.02	15.88 ± 0.03	15.25 ± 0.02
31	16h13m28.24s	-49d55m52.83s	−41.59 ± 1.77	0.37 ± 1.77	18.75 ± 0.04	17.74 ± 0.03	16.51 ± 0.01	15.83 ± 0.02	15.28 ± 0.02
32	16h14m49.50s	-49d08m25.29s	−12.99 ± 1.19	−28.31 ± 1.19	no detection	17.17 ± 0.02	16.17 ± 0.01	15.53 ± 0.01	14.96 ± 0.01
33	16h57m22.73s	-45d28m53.90s	−16.18 ± 2.94	−28.16 ± 2.90	18.29 ± 0.02	17.98 ± 0.03	16.70 ± 0.02	16.06 ± 0.02	15.54 ± 0.04
34	17h02m32.91s	-43d39m44.07s	−38.69 ± 0.71	−71.59 ± 0.68	17.49 ± 0.02	16.44 ± 0.02	15.42 ± 0.01	14.79 ± 0.01	14.34 ± 0.01
35	17h03m42.52s	-34d42m48.01s	−32.91 ± 0.93	−105.08 ± 0.84	16.13 ± 0.01	15.03 ± 0.01	14.04 ± 0.01	13.41 ± 0.01	12.93 ± 0.01
36	17h04m45.96s	-33d42m24.59s	26.36 ± 1.53	−38.03 ± 1.44	no detection	17.27 ± 0.05	16.32 ± 0.02	15.68 ± 0.02	15.18 ± 0.01
37	17h05m08.97s	-34d13m29.13s	−14.94 ± 0.79	−56.84 ± 0.72	17.24 ± 0.04	16.15 ± 0.02	15.15 ± 0.01	14.54 ± 0.01	14.04 ± 0.01
38	17h05m13.60s	-32d58m02.88s	−130.16 ± 2.47	−175.96 ± 2.69	no detection	17.87 ± 0.08	16.77 ± 0.04	16.08 ± 0.04	15.50 ± 0.02
39	17h12m23.41s	-39d30m31.78s	2.72 ± 2.20	−33.23 ± 2.15	19.06 ± 0.08	17.61 ± 0.04	16.45 ± 0.04	15.79 ± 0.04	15.31 ± 0.01
40	17h13m12.92s	-32d28m32.86s	−3.43 ± 0.81	−29.98 ± 0.80	18.25 ± 0.10	16.84 ± 0.05	15.79 ± 0.02	15.12 ± 0.03	14.55 ± 0.01
41	17h18m22.82s	-33d44m32.06s	−6.20 ± 1.26	−35.81 ± 1.29	18.11 ± 0.06	17.14 ± 0.04	16.15 ± 0.02	15.49 ± 0.03	14.99 ± 0.01
42	17h30m37.71s	-31d15m50.82s	19.31 ± 4.92	27.99 ± 7.17	18.64 ± 0.07	17.68 ± 0.07	16.64 ± 0.06	16.02 ± 0.10	15.45 ± 0.03
43	17h39m44.86s	-25d29m35.23s	−9.32 ± 1.16	−30.97 ± 1.07	no detection	17.62 ± 0.14	16.60 ± 0.09	15.90 ± 0.10	15.46 ± 0.02
44	17h45m26.66s	-37d51m25.44s	−4.09 ± 2.63	−36.01 ± 2.30	no detection	18.36 ± 0.09	17.13 ± 0.06	16.41 ± 0.05	15.69 ± 0.03
45	17h48m01.86s	-25d05m07.16s	−3.87 ± 5.95	31.48 ± 5.57	18.65 ± 0.07	17.83 ± 0.08	16.85 ± 0.07	16.21 ± 0.11	15.76 ± 0.04
46	17h49m06.94s	-36d51m08.38s	32.00 ± 1.73	−3.53 ± 1.75	no detection	17.85 ± 0.11	16.76 ± 0.06	16.09 ± 0.05	15.61 ± 0.02
47	17h55m08.10s	-26d09m52.35s	27.39 ± 6.94	−16.66 ± 4.96	19.23 ± 0.09	18.53 ± 0.10	17.47 ± 0.09	16.76 ± 0.15	15.46 ± 0.03
48	17h57m43.31s	-27d12m00.55s	−8.15 ± 5.00	29.01 ± 4.98	18.46 ± 0.04	17.57 ± 0.05	16.44 ± 0.04	15.74 ± 0.08	15.21 ± 0.03
49	17h58m05.75s	-22d22m40.24s	−6.88 ± 1.07	−36.70 ± 0.96	18.17 ± 0.06	16.80 ± 0.03	15.59 ± 0.02	14.90 ± 0.03	14.26 ± 0.02
50	17h59m48.74s	-38d23m42.73s	4.22 ± 2.07	−43.26 ± 2.14	19.71 ± 0.18	18.25 ± 0.07	16.93 ± 0.03	16.27 ± 0.03	15.75 ± 0.03
51	18h01m33.73s	-36d23m14.83s	110.07 ± 1.19	−45.15 ± 1.11	17.86 ± 0.07	16.71 ± 0.03	15.45 ± 0.01	14.71 ± 0.01	14.14 ± 0.01
52	18h07m53.34s	-23d52m31.76s	−27.55 ± 3.98	−13.57 ± 5.37	19.23 ± 0.16	18.50 ± 0.14	17.41 ± 0.07	16.71 ± 0.10	16.24 ± 0.04
53	18h08m04.69s	-30d49m48.21s	4.52 ± 1.56	−159.96 ± 1.39	18.42 ± 0.15	17.21 ± 0.07	16.07 ± 0.04	15.42 ± 0.03	14.95 ± 0.02
54	18h08m47.63s	-41d05m48.12s	64.62 ± 2.08	−92.96 ± 2.16	19.67 ± 0.10	18.36 ± 0.06	17.11 ± 0.03	16.38 ± 0.03	15.86 ± 0.03
55	18h08m47.83s	-39d37m13.31s	−39.50 ± 1.60	6.06 ± 1.70	18.90 ± 0.06	17.70 ± 0.04	16.57 ± 0.02	15.93 ± 0.02	15.49 ± 0.02
56	18h10m00.54s	-22d47m57.70s	8.63 ± 5.82	−30.12 ± 5.25	18.29 ± 0.07	17.70 ± 0.08	16.68 ± 0.08	16.07 ± 0.07	15.56 ± 0.03
57	18h18m16.64s	-37d19m25.14s	46.95 ± 2.72	−10.24 ± 2.75	no detection	18.23 ± 0.06	17.14 ± 0.03	16.54 ± 0.03	16.08 ± 0.04
58	18h18m38.76s	-25d46m57.16s	−3.82 ± 0.81	−160.03 ± 0.80	17.33 ± 0.05	16.07 ± 0.02	15.03 ± 0.01	14.36 ± 0.01	13.88 ± 0.01
59	18h20m27.96s	-34d55m43.14s	−5.03 ± 1.82	−105.83 ± 1.82	no detection	18.41 ± 0.07	17.24 ± 0.03	16.54 ± 0.04	16.00 ± 0.03
60	18h26m33.50s	-33d41m38.14s	−44.20 ± 0.99	−94.78 ± 0.81	17.09 ± 0.01	15.89 ± 0.01	14.73 ± 0.01	14.01 ± 0.01	13.42 ± 0.01
61	18h31m29.45s	-31d20m59.25s	9.88 ± 2.77	45.65 ± 2.87	19.57 ± 0.17	18.59 ± 0.15	17.19 ± 0.03	16.59 ± 0.04	16.09 ± 0.03
62	18h33m03.03s	-24d59m43.50s	−100.62 ± 1.42	6.04 ± 1.43	18.80 ± 0.07	17.53 ± 0.04	16.31 ± 0.01	15.64 ± 0.02	15.14 ± 0.02
63	18h33m37.76s	-29d14m41.82s	−16.98 ± 3.54	−35.71 ± 3.12	no detection	18.80 ± 0.10	17.46 ± 0.04	16.77 ± 0.04	16.31 ± 0.05
64	18h33m54.03s	-29d50m28.24s	20.71 ± 1.69	−22.90 ± 1.78	18.78 ± 0.07	17.62 ± 0.04	16.70 ± 0.02	16.09 ± 0.02	15.64 ± 0.02
65	18h34m17.26s	-27d54m07.63s	9.21 ± 1.32	−138.51 ± 1.10	15.82 ± 0.01	14.58 ± 0.01	13.62 ± 0.01	13.01 ± 0.01	12.51 ± 0.01
66	18h40m49.60s	-24d51m33.20s	−13.96 ± 2.04	37.16 ± 2.03	19.06 ± 0.08	18.02 ± 0.05	16.97 ± 0.03	16.36 ± 0.03	15.91 ± 0.04

Table D2. Early L dwarf candidates from our proper motion catalogue selected based on $\mu > 30$ $mas\ yr^{-1}$ and NIR colours.